Modeling of Al Evaporation and Marangoni Flow in Electron Beam Button Melting of Ti-6Al-4V

by

Zhongkui Zhang

B.Eng., Huazhong University of Science and Technology, 2009

A THESIS SUBMITTED IN PARTIAL FULFILLMENT
OF THE REQUIREMENTS FOR THE DEGREE OF

MASTER OF APPLIED SCIENCE

in

THE FACULTY OF GRADUATE STUDIES

(Materials Engineering)

THE UNIVERSITY OF BRITISH COLUMBIA
(Vancouver)

February 2013

Abstract

The Electron Beam Cold Hearth Remelting (EBCHR) process has emerged as a key process in producing high quality Ti-6Al-4V ingot and electrode as it is able to effectively consolidate both sponge and scrap material while removing undesired impurities and inclusions, such as Low Density Inclusions (LDIs) and High Density Inclusions (HDIs). However, the challenge of composition control arises in processing alloys such as Ti-6Al-4V where evaporative loss of elements with higher vapor pressure (Al in this case) cannot be ignored. Therefore, in order to cast a product of specified composition, a thorough understanding of the evaporation mechanism and melt flow conditions becomes crucial in process control and optimization.

This research presents a comprehensive model of the melt pool produced during Electron Beam Button Melting (EBBM) which has been developed to serve as an intermediate step in the development of a comprehensive tool for analysis and optimization of the industrial EBCHR process. With proper geometry and boundary conditions, the EBBM model can be readily applied to an industrial EBCHR furnace to minimize costly experiments in optimizing process parameters.

A thermal-fluid-compositional model has been developed that includes Al evaporation, thermal and compositional buoyancy, thermal and compositional Marangoni flow and flow attenuation in the mushy regime. Experiments on Ti-6Al-4V and CP titanium with a circular electron beam pattern were conducted in a laboratory scale EBBM furnace in order to study the evaporation process and fluid flow in the liquid pool. The data obtained from the

experimental work was used to tune the thermal boundary conditions and validate the model predictions. The temperature, surface velocity, pool profile and concentration profile have been experimentally quantified and used for validation of the mathematical model.

Table of Contents

List of Tables

List of Figures

Acknowledgments

I would like to thank Dr. Daan Maijer and Dr. Steve Cockcroft for their patient guidance and enormous help in the research, for the shared expertise and professionalism, and also for the valuable opportunities they have provided to attend seminars and conferences.

Dr. Carl Reilly, with his extensive knowledge in mechanical engineering, helped to design and install the devices for measuring velocity and temperature. His effort in maintaining and modifying the electron beam furnace is also deeply appreciated. As it turns out, experiments with the EB furnace require a collaborative effort. Without him, it simply would not have been possible to finish all the experiments within the time available for this project.

I appreciate Dr. Ainul Akhtar's valuable advice in servicing the electron beam gun and preparing the samples. Mr. Wonsang Kim, the department's electronics technician, has made a great contribution by undertaking maintenance and repair of the EB furnace when required.

My thanks to Mr. Carl Ng, Mr. David Torok and Mr. Ross McLeod for machining test samples, and to Dr. Lu Yao and Mr. Jacob Kabel for assisting me with the SEM/EDX measurements. Thank my colleagues: Miss Jianglan (Holly) Duan, Mr. Jun (Eric) Ou and Mr. Aniruddha Chatterjee for the discussion and support both in conducting the experiments and building the numerical model.

Finally, I would like to thank my family for their constant love and support. I never would have made it here without you.

Chapter 1

Introduction

1.1 Titanium Alloy Production

Titanium and its alloys are utilized in a variety of industries, including the aerospace, chemical, biomedical and automotive industries. This is primarily due to its properties such as excellent strength to weight ratio, outstanding corrosion resistance, superior biocompatibility and high melting temperature (1668 ^{o}C for Commercially Pure Titanium or CP Ti[1]). Despite having excellent corrosion resistance in a wide variety of applications provided by a highly stable surface oxide film, titanium is highly reactive with oxygen and nitrogen at elevated temperatures and in particular in the liquid state. Therefore liquid metal processing must be carried out under vacuum or in an inert atmosphere. Autogenous containment is also necessary to prevent molten titanium from reacting with the materials forming the holding vessel[2]. Water-cooled copper is commonly used to form a solid shell of titanium to realize this containment.

Titanium is usually extracted from rutile (TiO_2) or ilmenite ($FeTiO_3$)[3]. After extraction and purification via the Kroll process, the metal has a porous structure and is referred to as sponge. A further consolidation step is required to produce primary ingot from the sponge. In addition to the Kroll process, the extra consolidation step makes the production

of titanium not only difficult but also expensive in comparison to Al-based, Fe-based and some Ni-based alloys. Therefore, the ability to recycle titanium scrap is necessary to make titanium production more cost-effective[4].

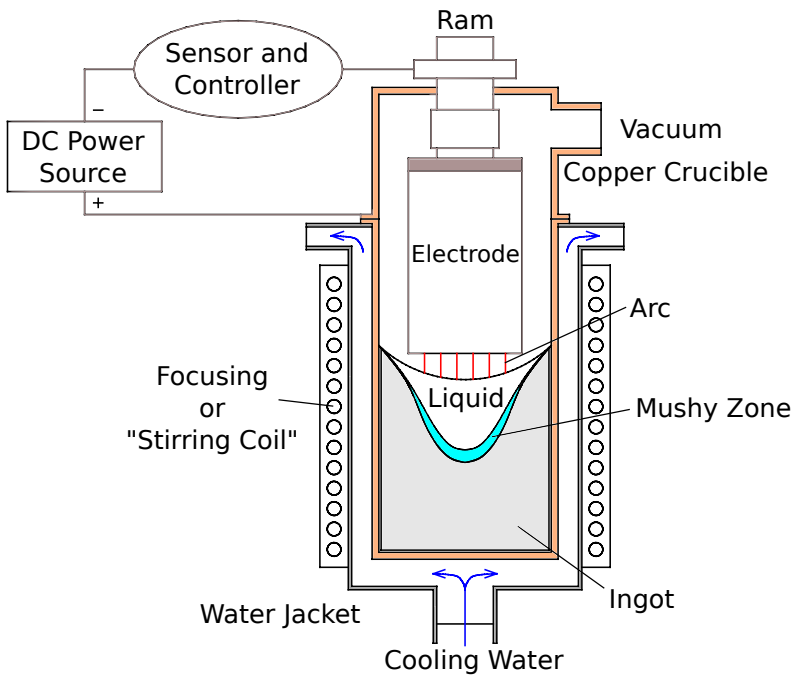

(a) Schematic of VAR Furnace and Ingot. After [3]

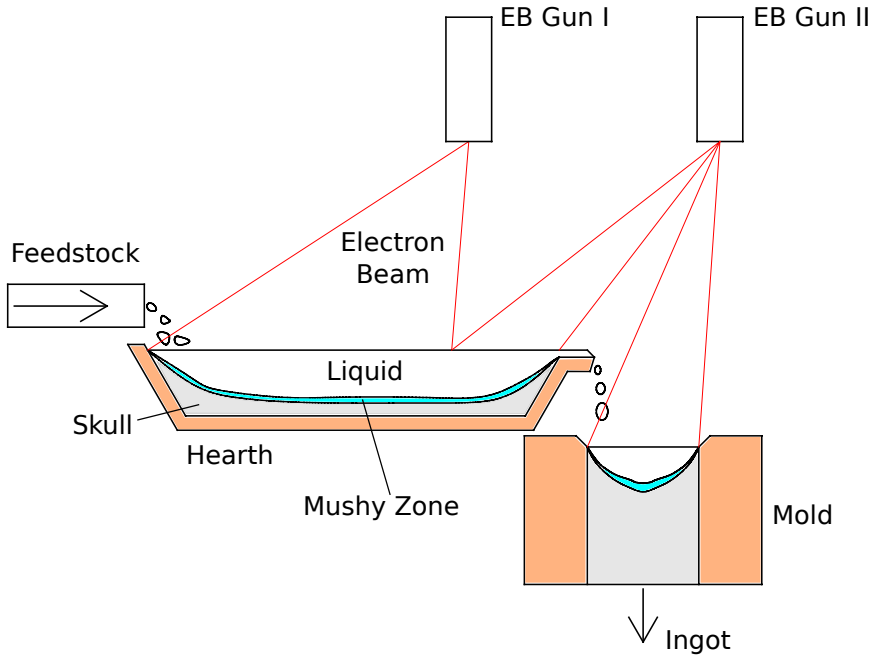

(b) Schematic of EBCHR. After [4]

Figure 1.1: Schematics of VAR and EBCHR Processes

The two main commercial consolidation methods are: Vacuum Arc Remelting (VAR) and Cold Hearth Remelting (CHR)[5]. In the VAR process, an electrode is first made by mechanically compacting and welding sponge and alloying elements together. In the second step, the electrode is melted and cast in water-cooled copper crucible to form an ingot, as shown in Figure 1.1(a). The CHR process in contrast uses either electron beam (EB) guns or plasma torches as heat sources to first melt feedstock in a water-cooled copper hearth prior to solidification in a water-cooled copper mold. Figure 1.1(b) shows a typical Electron Beam Cold Hearth Remelting (EBCHR) process where the raw material is melted on one side of a water-cooled copper hearth. The molten metal flows along the refining hearth and into a water-cooled mold where it is cast as a primary ingot.

Depending on the quality requirement of the primary ingot, either single application or multiple applications of one or more of the consolidation methods may be specified. For example, for aero-engine disk grade material, the highest quality specification, either a triple VAR or a combination of CHR and VAR may be used, depending on the preference of the customer. In those cases where a CHR process is specified, a VAR melt is required as a final processing step to achieve chemical homogenization and improve the structure[5].

1.2 Melt-related Defects

The common melt-related defects identified in titanium alloys are: High Density Inclusions (HDIs) and Low Density Inclusions (LDIs)[6]. HDIs, such as tungsten carbide tool bits, incandescent light filaments, tips from ball-point pens, thermocouple scrap and pieces of Tungsten Inert Gas (TIG) welding electrode, are occasionally introduced with revert feedstock[7]. LDIs, also known as Hard Alpha, Type I defects or High Interstitial Defects (HIDs), originate from high concentrations of alpha stabilizers (N, O, C) and can be present in both revert feedstock and virgin titanium sponge. The locally stabilized alpha phase acts as a potential crack initiation site in the matrix material as it is comparatively very hard and brittle. Another type of LDI defect are Al-rich regions, known as Type II

alpha defects, which also lead to crack initiation in titanium because of their comparatively lower yield point than the surrounding matrix material. Finally, beta stabilizing elements, such as Fe, Cr, Mn, Ni and Cu, can segregate during solidification and are another source of defects. The resultant solute rich regions are called beta flecks because of their distinctive microstructure[3].

Any of the aforementioned defects have the potential to cause component failure, which can be catastrophic and cause loss of life in aerospace applications. Therefore defect control is of utmost importance in the premium quality titanium manufacturing industry.

1.3 Electron Beam Cold Hearth Remelting

With regard to defect removal, EBCHR has several advantages over VAR due to the fact that the refining process is physically separated from the casting process (see Figure 1.1)[5]. Firstly, volatile elements such as chlorine and hydrogen are eliminated by the exposure to the high vacuum environment during transit in the refining hearth. Secondly, HDIs and LDIs are effectively removed by gravitational separation. HDIs settle to the bottom of the refining hearth and are trapped in the mushy zone due to their relatively high density, while LDIs can be removed by one or more mechanisms depending on their density relative to the density of the liquid metal, e.g., they can sink and be trapped in the mushy zone, they can be of neutral density and dissolve by virtue of the long residence time in liquid metal provided by the refining hearth or they can float and be melted by contact with the electron beam. In contrast, in the VAR process there is no method to guarantee the removal of HDI's (hence the triple VAR specification for aero-engine disk material). Thus, the EBCHR process is emerging as an attractive addition to traditional VAR melt shops for its ability to treat revert.

Another advantage of the EBCHR process is its ability to produce ingots with different cross-sections, such as rounds, squares, slabs and bars. This flexibility can reduce the subsequent conversion loss and cost in rolling when flat products such as plates, sheets and strips are being produced[3].

The main disadvantage with the EBCHR process lies in the evaporation loss of alloying elements with relatively high vapor pressure, for example, Al and Cr. During steady state casting, chemistry control is relatively straightforward and is achieved by enriching the feedstock of the alloy or alloy additions prone to preferential evaporation. In contrast, during the final stage of ingot solidification, where feeding is stopped and the top surface of the ingot is kept molten to minimize shrinkage voids (known as hot-topping), loss of chemistry control can be a problem. If a prolonged hot top is applied, the high vapor pressure elements preferentially evaporate leaving a region of material with off-spec composition which has to be cropped[8]. Alternatively, too short of a hot top is carried out then the top surface of the ingot rapidly solidifies trapping a subsurface melt pool, which results in internal void formation due to solidification shrinkage. In the case of CP titanium ingots, the voids can be eliminated via downstream processing. Whereas, in the case of aluminum bearing alloys the void interior surface are enriched in aluminum, which can result in an aluminum-stabilized alpha stringers. Thus, the top section of ingots containing the voids must be cropped prior to downstream conversion.

In summary, the EBCHR process is an important consolidation process for producing titanium primary ingot because of its ability to treat both scrap and sponge material while guaranteeing the elimination of HDIs and LDIs. However, the propensity for evaporative loss of alloying elements with high vapor pressure can make controlling composition a challenge in this process, particularly during hot-topping. Therefore, an improved understanding of evaporation and its effect on heat transfer and fluid flow conditions is required for process design, control and optimization. The current research focuses on a lab scale electron beam button melting process and uses it as an experimental tool to develop a mathematical model that contributes to the understanding of Al evaporation and its influence in the electron beam melting of Ti-6Al-4V.

Chapter 2

Literature Review

According to the Langmuir equation, the evaporation of alloying element with high vapor pressure in the EBCHR process is principally affected by the temperature of the melt and the chemical activity of the volatile species at the point of interest on the surface of the melt. The chemical activity is in turn dependent on concentration. Thus an understanding of the thermal-fluid flow regime within the melt is required to correctly characterize the evaporation process. To this end, researchers have investigated evaporative losses during the EBCHR process using a variety of experimental and numerical methods.

2.1 Aluminum Evaporation

Considering all the potential kinetic factors, the process of aluminum evaporating from Ti-6Al-4V in a vacuum furnace occurs in three steps[9]:

(1) transport of aluminum through the bulk liquid to a boundary layer near the surface;

(2) transport of aluminum across the boundary layer to the surface;

(3) evaporation of aluminum from the surface into the vacuum chamber.

Ritchie[10] confirmed, through experiments, that the evaporation rate is not affected by the vapor when the chamber pressure is below 3 Pa. This assessment was based on the fact that

with operating pressures of 10^{-1} to 10^{-3} Pa and a chamber size smaller than twice the mean free path (1 mean free path $\approx$ 5-10 m), the vapor will reach the chamber wall freely. The chamber wall is usually water-cooled and cold enough that the vapor will condense and not return to the gas phase after the initial contact.

Isawa *et al.*[4] examined the Al concentration in the feedstock, the hearth and the ingot after conducting Ti-6Al-4V remelting experiments in a 250 kW EB furnace. It was found that the main Al evaporation site was the melt pool in the hearth. The time for evaporation during melting was too short to allow significant Al loss from the feedstock or from the metal drops, and the evaporation rate during casting was low because the temperature was maintained just above the liquidus temperature. It was also found that the Al concentration was almost homogeneous throughout the melt pool in the hearth, leading to the conclusion that there was complete mixing in the relatively small hearth (400 mm$\times$150 mm$\times$50 mm). However, as pointed out by Ritchie[10], the uniform composition may be caused by homogenization since the fluid conditions change dramatically from melting to solidification. Thus, a careful study of the fluid flow is necessary in determining the rate of bulk transport (step 1) and the rate of transport across any boundary layer that may or may not develop (step 2) in the EB remelting process.

Watakabe *et al.*[11] considered the loss of Al to be rate-limited by steps 2 and 3 during the melting of Ti-6Al-4V alloy. By adding pure Al to a Ti-6Al-4V melt to compensate for evaporative losses, they found that the removal of Al was rate-limited by step 3 when the Al concentration was greater than 6 wt% and by step 2 when the Al concentration was less than 6 wt%. The deposits on the furnace wall were also analyzed in their research. It was shown that the Al content was 54.8 wt% in the initial deposit and 25.4 wt% in the final deposit. The change of composition in the deposits led to the conclusion that the Al concentration in the melt was reduced to 3 wt% or less by the end of the experiment.

Nakamura and Mitchell[12] melted small Ti-6Al-4V cylinders (90 mm in diameter and 25 mm in height) in a 30 kW EB furnace and applied various beam-scanning frequencies

(0, 0.1, 1, 10 Hz) to study the effect of beam oscillation rate on aluminum evaporation. An electron beam power of 2 kW was used for preheating before rapidly increasing the power to 15.5 kW where it was maintained for a defined period (1, 5, 10 min) before being turned off. Concentration analysis showed that there was no gradient in Al concentration in the pool: In the 5 min experiments, 3.23 wt% was measured on the surface and 3.96 wt% in the pool; in the 10 min experiments, Al content was found to be 1-2.5 wt%. The total evaporation loss was also determined by comparing the sample weights before and after the experiment. It was found that increasing the beam oscillation rate (from 0 to 10 Hz) lead to decreased weight loss, however, the effect on weight percentage of Al was much less obvious because of the high ratio of Ti to Al in the samples.

Suzuki *et al.*[13] conducted experiments on melting and precision casting of Ti-6Al-4V in a 120 kW electron beam furnace. They obtained the temperature in the molten pool during these experiments using three methods: a two-color pyrometer, an estimation based on the evaporation rate and using type-C thermocouples. The temperature at the center of the pool's surface was measured to be 1902 ± 15 ^{o}C by the pyrometer. The temperature calculated from the evaporation rate was 1912 ± 15 ^{o}C and the temperatures 5 mm and 10 mm below the surface measured by thermocouples were 1722 ± 15 ^{o}C and 1667 ± 15 ^{o}C, respectively. These measurements were in good agreement considering the temperature gradient in the liquid pool (the pool depth was 30 mm and the expected liquidus temperature was 1650 ^{o}C). The composition of the condensate deposit was 58 wt% Ti, 38 wt% Al and 1 wt%V. The Al content in the molten pool was found to decrease significantly at the beginning of melting and reached 3 wt% in 5 minutes.

2.2 Surface Tension Driven Flow

Surface tension is dependent on temperature and concentration. Fluid is driven by surface tension to flow away from regions of low surface tension toward regions of high surface tension (Marangoni flow). Lee *et al.*[14] studied the thermal Marangoni effect during electron

beam button melting of IN718, in which sulfur was believed to be a surface active element. It was observed in the experiments that when the sulfur level was increased from low (6 ppm) to high (20 ppm) concentrations, the fluid flow direction on the surface of the melt pool changed from being radially outwards to radially inwards (as shown in Figure 2.1). Marangoni flow was observed to dominate the fluid flow in the molten pool. A coupled heat

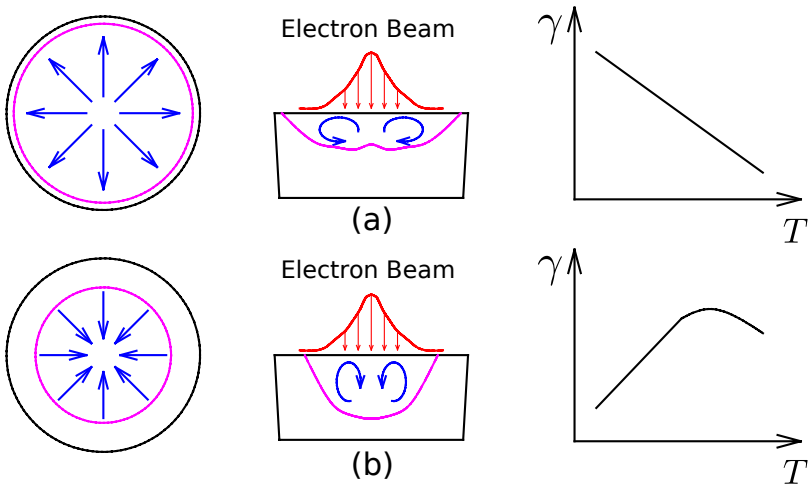

Figure 2.1: Melt Flow Patterns with: (a) Low Group VI Element Content; (b) High Group VI Element Content. After [14].

transfer and fluid flow model was developed to study the Marangoni effect. In the model, the surface tension coefficient was considered to be a function of temperature and to vary with sulfur content (Figure 2.1). The model predictions showed that the surface flow in the low sulfur case was outwards with a maximum velocity of 0.16 m/s, while in the high sulfur case, it was inwards with a maximum velocity of 0.14 m/s. In their experiment with a stationary electron beam, alumina particles were added as markers on the surface of the liquid pool in order to determine the surface velocity of the fluid. The maximum velocity observed in the inwards flow case was 0.19 m/s. In the outwards flow case however, the particles in the high velocity region could not be traced and the maximum velocity in the regions where the particles were visible was 0.06 m/s. It was concluded that surface tension driven flow is dominant in the electron beam button melting process and therefore its proper description is crucial in predicting mushy zone size and molten pool profile.

Paradis *et al.*[15] measured the surface tension of liquid titanium using the oscillating droplet method in a vacuum electrostatic levitation furnace. The values were reported as a function of temperature as:

$$\gamma(T) = 1.557 - 1.56 \times 10^{-4}(T - T_m), \quad 1750 \text{ K} \leq T \leq 2050 \text{ K} \tag{2.1}$$

where γ (N/m) is the surface tension, T (K) is the temperature and T_m (K) is the melting point of titanium (1943 K).

Aune, Egry, Wunderlich *et al.*[16–18] conducted measurements of surface tension of Ti-6Al-4V using the same method on board parabolic flights. The surface tension function determined through these investigations was:

$$\gamma(T) = 1.49 - 4.1 \times 10^{-4}(T - T_L), \quad 1773 \text{ K} \leq T \leq 2173 \text{ K} \tag{2.2}$$

where T_L (K) is the liquidus temperature of Ti-6Al-4V (1933 K). This result was found to agree well with their previous ground-based measurements of:

$$\gamma(T) = 1.33 - 3.6 \times 10^{-4}(T - T_L) \tag{2.3}$$

As a highly surface active element, oxygen can significantly decrease the surface tension in molten metal even at very low concentrations[19]. Wunderlich *et al.*[18] compared surface tension measurements for Ti-6Al-4V samples with low oxygen (0.047 wt%) and high oxygen (0.096 wt%). It was found that the surface tension of the high oxygen sample at 2073 K was 15% lower than the low oxygen sample.

Lei *et al.*[20] modeled laser surface remelting of type 304 stainless steel using a fixed-domain continuum model. The competitive influence of thermal Marangoni flow and evaporation on the surface temperature and pool shapes was examined. The results showed that when the absolute value of the surface tension coefficient exceeds 3.0×10^{-4} N/m/K, the

heat loss by laser-induced evaporation of alloying elements is negligible and therefore can be ignored. However, evaporation was found to affect surface temperature and pool profile significantly when the absolute value of surface tension coefficient is low and buoyancy driven flow is dominant over Marangoni flow.

2.3 Modeling of Electron Beam Melting

Semiatin *et al.*[21, 22] analyzed evaporation of Al from Ti-6Al-4V during EBCHR by solving a one-dimensional diffusion equation. Continuous and laminar flow was assumed in the refining hearth and the following equation was used to define the diffusivity for aluminum in liquid titanium in the analytical solution to the diffusion equation:

$$D = 1 \times 10^{-8} e^{\frac{250000}{R}\left(\frac{1}{T_{liq}} - \frac{1}{T}\right)} \tag{2.4}$$

where D (m^2/s) is the diffusivity, R ($\mathrm{J/kg/K}$) is the gas constant, T_{liq} (K) is the liquidus temperature (1925 K for Ti-6Al-4V), and T (K) is the temperature of the melt pool estimated by the following heat balance:

$$A\varepsilon\sigma T^4 \approx 0.7 \times W_e - W_h - W_{metal} \tag{2.5}$$

where A (m^2) is the area, ε (equal to 0.5) is the melt surface emissivity, σ ($\mathrm{W/m^2/K^4}$) is the Stefan-Boltzmann constant, W_e (W) is the power of the electron beam gun, W_h (W) is the heat loss through conduction, and W_{metal} (W) is the heat of fusion. The model predictions of final composition were correlated with experimental results found in the literature. A sensitivity analysis showed that aluminum evaporation loss was strongly affected by the diffusivity. Without considering the temperature and fluid flow variations in the pool, Equation 2.4 represents an enhanced diffusivity that accounts for the effect of mixing in the hearth. Akhonin *et al.*[9] developed a similar model by dividing the aluminum evaporation

process into three steps: diffusion across the boundary layer, transfer through the interface and evaporation to the vacuum environment. Their model predictions demonstrated that both increasing casting rate and decreasing beam power will reduce aluminum evaporative losses. It was also found that the initial aluminum content in the feedstock has a significant effect on the final composition of the ingot.

By developing a model based on a modified low Reynolds number, $k-\varepsilon$ turbulence algorithm, Shyy and Pang *et al.*[23] investigated the effects of turbulence on ingot casting in the EBCHR process. In the process studied, molten Ti-6Al-4V was poured continuously into a water-cooled copper mold with an inner diameter of 0.432 m and a height of 0.457 m. Turbulent flow was observed in the experiment and examined in the model under two casting speeds: 2×10^{-4} m/s (455 kg/hr) and 4×10^{-4} m/s (910 kg/hr). Darcy's flow resistance, thermal buoyancy and thermal Marangoni flow were all included in the model. The modeling results showed that turbulence reduced temperature gradients in the melt by enhancing the transport of heat in the mushy zone and the thickness of the mushy zone varied significantly with the presence of turbulent flow.

Tripp[5] investigated the power transfer in the electron beam melting process at both the laboratory and industrial scales. In laboratory experiments, CP titanium cylinders instrumented with thermocouples were melted to examine the effect of chamber pressure on the thermal regime developed in the cylinders. Tantalum cylinders were heated using the same procedure for titanium to study this effect without generating a liquid pool or vapor phase. A finite element heat transfer model was developed where the thermal conductivity for liquid titanium was increased (multiplied by 20) to represent the enhanced heat transfer caused by fluid flow. The inverse heat transfer method was adopted to calculate the electron beam heat flux distribution. The results showed that the electron beam heat flux pattern could be fit with a Gaussian distribution in which the spreading parameter σ (mm) was dependent on the experimental conditions such as target materials and chamber pressure p (Pa). The relationships determined for σ are listed below:

For tantalum,

$$\sigma = \begin{cases} 6.4 & p < 0.37, \\ 12.64 - 33.265p + 44.276p^2 & 0.37 \leq p \leq 0.93. \end{cases} \tag{2.6}$$

For CP titanium,

$$\sigma = \begin{cases} 121.4209p^2 - 40.5255p + 19.5132 & p < 0.2, \\ 0.6921p^2 - 7.7660p + 14.6840 & 0.2 \leq p \leq 0.8. \end{cases} \tag{2.7}$$

In the industrial scale experiments however, the relationship between electron beam power distribution and chamber pressure did not correlate with observations. The difference between laboratory and industrial experimental conditions such as higher beam accelerating voltage, longer beam traveling distance and more complex fluid flow patterns was cited as the reason for the lack of correlation.

High electron beam pattern scanning frequencies are usually preferred in industrial furnaces to avoid high temperature fluctuations and localized evaporation of volatile elements[14]. Powell *et al.*[24] summarized the effect of beam-scanning frequency (alternating line scanning pattern with a total length of 2.4 m) on the evaporation loss in the electron beam melting of CP Ti and Ti-6Al-4V as: (1) At frequencies above 400 Hz, the power distribution over the scan pattern may be considered uniform because of the extremely short dwell time; (2) At frequencies between 60 and 400 Hz, evaporation rates will be affected by temperature fluctuations although transients in fluid flow due to thermal cycling are not significant; (3) At frequencies between 20 and 60 Hz, evaporation rates are affected by thermal Marangoni flow; and (4) At frequencies below 20 Hz, turbulent flow, jet evaporation (ablation) and other phenomena may affect surface temperatures. In their simulations, increasing beam-scanning frequency was shown to reduce the evaporation rates, assuming that the electron beam deflection system was capable of maintaining the beam patterns.

Bellot *et al.*[25] modeled the evaporation of aluminum during the electron beam melting of Ti-6Al-4V in a cold hearth. The effect of turbulence was considered by using a mixing length model to predict the turbulent viscosity. Turbulent conductivity and diffusivity were estimated by using turbulent Prandtl and Schmidt numbers equal to one. Buoyancy was included in the model by applying a Boussinesq approximation, in which thermal and compositional expansion coefficients were introduced in a gravitational source term in the momentum equation. The thermal Marangoni effect was calculated by adding a shear force to the pool surface. However, compositional Marangoni effects were not included in the model since only a slight change in the aluminum content (from 6 wt% to 5.3 wt%) was observed in the ingot. Analysis of the evaporative loss of aluminum indicated that the Langmuir equation was adequate for calculating the mass flux due to evaporation. A high casting rate was shown to slightly reduce evaporative losses, while an increase in beam-scanning frequency from 0.5 to 11 Hz decreased the aluminum loss by 10%.

Ritchie *et al.*[10, 26] studied the evaporation process during the electron beam button melting of AISI 316 stainless steel using both experimental and numerical methods. The instantaneous composition of the liquid pool was calculated from x-ray data acquired by an Energy Dispersive X-ray (EDX) spectrometer and compared with the average values determined by analyzing collected vapor deposit samples. A lower content of volatile elements was found in the vapor deposit samples. A mathematical model of momentum, heat and mass transfer was developed and the flow pattern in the liquid pool was shown to be a recirculating cell with fluid moving radially outwards on the pool surface. It was thus concluded that the evaporation of volatile elements was controlled by Langmuir evaporation and the process was dominated by surface temperature.

Zhao[8] developed a coupled thermal-fluid model to study the electron beam casting of large industrial Ti-6Al-4V ingots (1.3716 m$\times$0.6731 m$\times$1.5240 m) using a commercial CFD (Computational Fluid Dynamics) software, ANSYS CFX 10.0. The model included the release of latent heat, thermal buoyancy and flow attenuation in the mushy zone. An

analysis of the overall heat balance of the model revealed that the energy input to the casting process is dominated by the incoming molten titanium (65%) compared with the electron beam (35%). Energy is lost from the casting process through radiation and evaporation from the top surface (31%), through the out flow of solid metal at the bottom boundary of the domain(24%), through contact with the mold (29%) and through radiation to the surrounding environment (16%). A predicted pool depth of 0.8 m was found to agree well with industrial experimental results. A sensitivity analysis on the casting parameters showed that the pool depth was more affected by casting rate than beam power, while the effect of superheat temperature of the incoming liquid metal was found to be negligible.

Meng[27] examined the factors contributing to fluid flow and heat transfer in the electron beam button melting of Ti-6Al-4V including thermal buoyancy, thermal Marangoni flow and flow attenuation in mushy zone. It was concluded that the thermal Marangoni force drives the flow from the high to low temperature regions creating a wide and shallow liquid pool with recirculating flow. Thermal buoyancy was seen to have a similar effect but to be larger in magnitude. The presence of mushy zone flow resistance was seen to dampen the effects of the above-mentioned driving forces. The pool profile was shown to be affected more by beam power and cooling conditions than beam-scanning frequency by a sensitivity analysis.

In summary, aluminum evaporation in the EBCHR of Ti-6Al-4V has been investigated and its effect on the composition of the melt characterized. Although surface tension driven flow has been observed as dominant in the molten pool under certain conditions, further study is necessary to determine the relative contributions of thermal Marangoni, compositional Marangoni, thermal buoyancy and compositional buoyancy on the thermal and compositional fields during electron beam melting of Ti-6Al-4V.

Chapter 3

Scope and Objectives

The main objective of this program (Master of Applied Science) is to develop a comprehensive model to describe the evaporation of aluminum during the Electron Beam Button Melting (EBBM) of Ti-6Al-4V. In EB-based melt processing of Ti-6Al-4V, the high evaporation rate of aluminum in the vacuum environment has the potential to result in compositional variability in the final product. The ability to predict compositional variations hinges on understanding the mass, momentum and energy transport processes occurring in the melt pool. The drivers for these processes include thermal and compositional gradients, which result in buoyancy forces that act throughout the melt pool and Marangoni (surface tension) forces that act on the melt surface.

The complexity of physics involved in the EB melting process will be described numerically by developing a coupled thermal-fluid-compositional model capable of accounting for the evaporation of aluminum and the mass transfer in the molten pool. The equations of mass, momentum and energy will be solved for the velocity and temperature fields, while the aluminum concentration is tracked in the model by solving an additional transport equation. Buoyancy will be implemented by introducing a source term to the momentum equation with density varying with both temperature and Al concentration. Marangoni flow will be modeled by applying a shear force in the momentum boundary condition at the pool surface.

Coefficients describing the variation in surface tension with both temperature and Al concentration can be used to determine the shear force. Additional factors to be incorporated into the model include the release of latent heat, that will be incorporated by modifying the specific heat as a function of temperature using the Effective Specific Heat method, and flow dampening in the two-phase mushy zone, that can be accounted for by applying Darcy's Law as a source term in the momentum equation.

The second objective of the project is to verify the model through lab-scale experiments conducted in an Electron Beam Button Furnace. The experiments will be used to provide data suitable to verify the model. The data will include the temperature distribution, as inferred from both the liquid pool profile and measurements at discrete locations within the button sample, the surface velocity, as inferred from tracking particle markers added to the surface, and concentration profile, as measured in the final solidified button sample. In addition, thermocouples will be used to measure cooling curves at defined locations in the sample, including within the liquid pool and mold to validate the thermal boundary conditions applicable to the button.

Finally, the model will be used to assess the effect of aluminum evaporation on the flow conditions and pool profile. This information will be critical in assessing which factors are crucial in the development of models to simulate the hearth refining process and casting process associated with industrial Electron Beam Cold Hearth Remelting (EBCHR) technology.

Chapter 4

Experimental Procedure

A series of electron beam melting experiments were conducted using the laboratory scale Electron Beam Button Furnace (EBBF) at the University of British Columbia (UBC). The measurements from these experiments were used to characterize the boundary conditions and to verify a thermal-fluid-compositional model of the button. The boundary conditions tuned with this data include the top surface, which involves the EB heat flux, losses associated with radiation and evaporation, and the button/mold interface, which includes the side wall and bottom face. As part of the process, modeling results were compared with experimentally determined cooling curves, surface velocities, pool profiles and concentration profiles.

4.1 Electron Beam Button Furnace

The EBBF at UBC consists of an electron beam gun, a furnace chamber, a vacuum system, a cooling system, a control system, a power supply and auxiliary equipment, as shown in Figure 4.1.

The furnace is equipped with a Von Ardenne EH-30/20 electron beam gun capable of generating an electron beam with a power of up to 30 kW using an acceleration voltage of 20 kV[28]. The EB gun has a power control panel and a beam control module. The power

control panel regulates the current and voltage for the three components of an EB gun circuit: the filament, the exciter and the beam. These currents and voltages are manually adjusted via the dials on the panel. The beam control module is connected to the beam guidance and deflection system for the EB gun, which accepts external signals to manipulate the trajectory of the beam. It also allows manual adjustment of the focus and position of the beam spot.

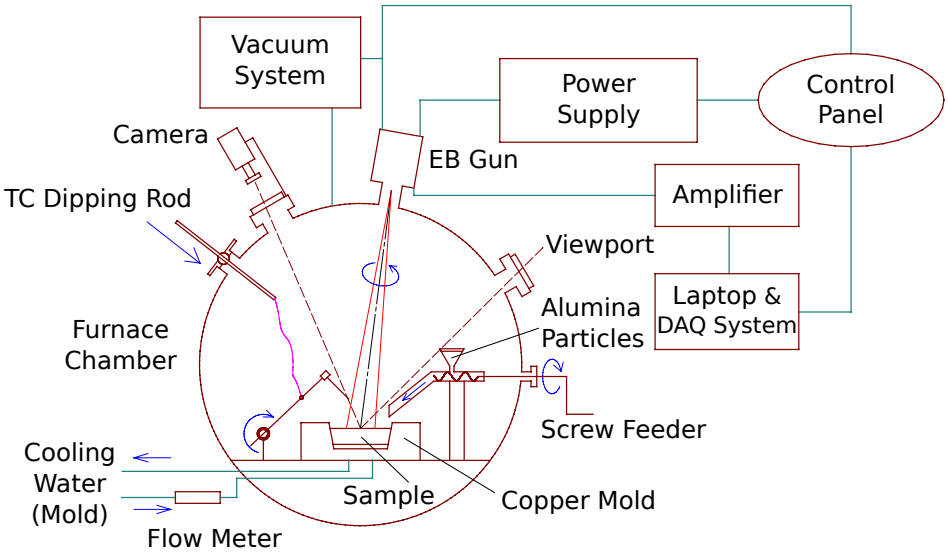

Figure 4.1: Diagram of the Electron Beam Button Furnace

The furnace vacuum chamber has multiple ports as shown in Figure 4.1. There is a viewport on the chamber door for direct observation of the interior of the furnace and a second viewport on the top of the chamber where a high-speed machine vision video camera is mounted. Both of these viewports are protected by disposable acetate film and replaceable optical glass. During experiments, metal vapor deposits on the furnace wall and the acetate film. The observation port is kept closed when not in use to avoid excessive vapor deposition on the acetate film. To maintain a clear vision for the camera, the acetate film in the camera port is continuously rolled across the optical glass. One of the access ports mounted on the side of the furnace has a ball joint that allows some manipulation of a rod that can be inserted through it without degrading the vacuum. This port is used during experiments to dip a thermocouple into the liquid pool of the button. An auger-shaped screw feeder was

also installed in the chamber on a second access port to feed alumina particles onto the liquid pool surface. The feeding of alumina particles was manually controlled by a handle outside of the chamber.

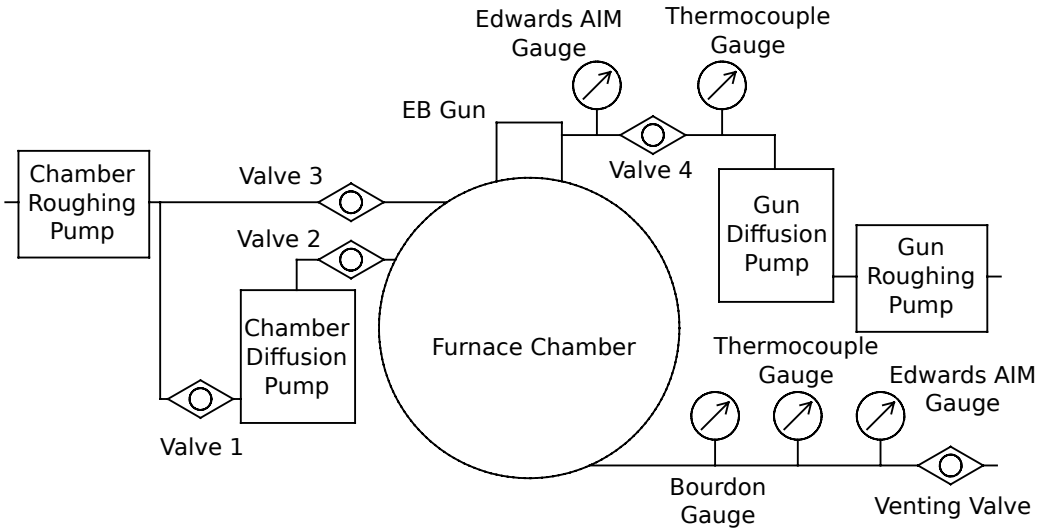

Figure 4.2: Diagram of the Vacuum System

Table 4.1: Pressure Gauges Used in the Vacuum System

Gauge Type	Quantity	Range (mbar)
Bourdon Gauge	1	10^3 — 1
Thermocouple Gauge	2	1 — 10^{-3}
Edwards AIM Gauge[1]	2	10^{-2} – 10^{-8}

[1] Model: Edwards AIM-S-NW25.

The EB gun and the furnace chamber have their own vacuum pumping systems, as shown in Figure 4.2. Each vacuum pumping system is composed of a roughing pump, a diffusion pump, and multiple valves and gauges. The roughing pumps are rotary vane pumps, which evacuate the vacuum system to a given pressure and are used as backing pumps for the diffusion pumps. The diffusion pumps have their own heating and cooling components, which circulate silicone oil to extract gas molecules and therefore enable high vacuum pumping. The various valves are used to control the sequence of vacuum pumping and the gauges are switched according to the vacuum levels. The type and range of the

gauges are summarized in Table 4.1. Under typical operating conditions, a vacuum level of 8×10^{-6} mbar (8×10^{-4} Pa) can be reached in the EB gun chamber and 5×10^{-5} mbar (5×10^{-3} Pa) in the furnace chamber[29].

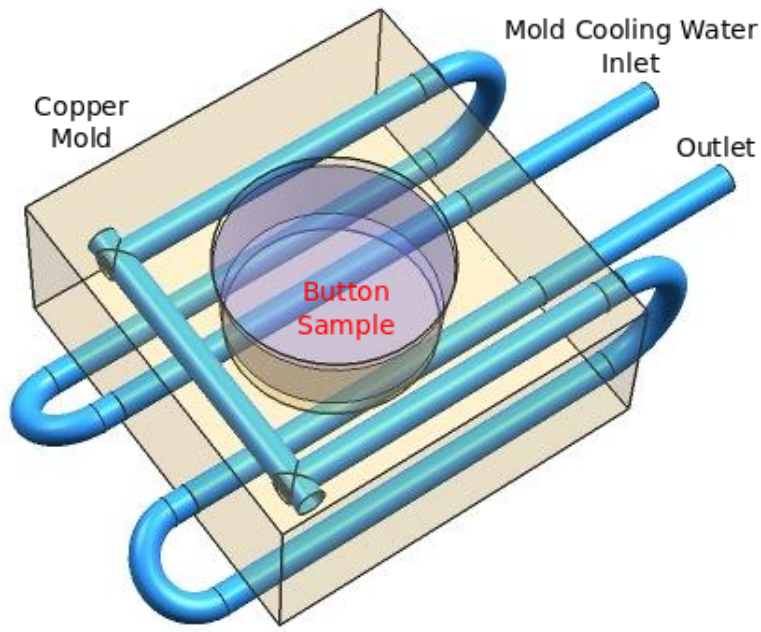

(a) 3D Drawing of the Copper Mold

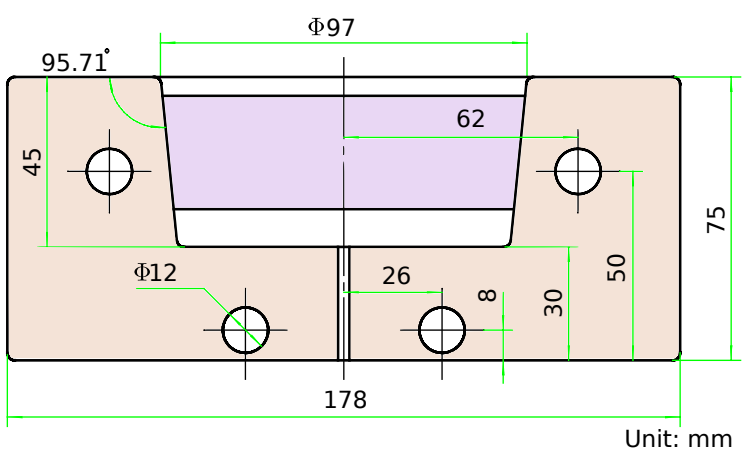

(b) Dimensions of the Copper Mold

Figure 4.3: Drawing and Dimensions of the Copper Mold Used in the Experiment

A drawing of the water-cooled copper mold used in the current experiments is shown in Figure 4.3. For the setup shown in Figure 4.3, heat is extracted from the button to the mold through the bottom face via radiation and through the side wall via a combination of contact

conduction and radiation. On the top of the sample, heat is lost to surrounding furnace chamber via radiation and via evaporation if significant for the alloy being melted. Heat is input to the top surface via the electron beam, with the amount and distribution dependent on the gun control parameters. The geometry of the button and mold with respect to the taper of the sidewalls was designed to result in a gap between the bottom of the button and the mold. This was intended to reduce heat transfer and maximize the depth of the molten pool. The degree of contact between the button and the mold on the side wall can be affected by the relative thermal expansion of the button and mold when heat is applied and the temperature increases. Hence the effective interfacial heat transfer will in general be a function of temperature.

4.2 Data Acquisition

4.2.1 Data Acquisition System

Two data acquisition systems (USB-1208HS-4AO and USB-2416-4AO manufactured by Measurement Computing Corp.) were connected to a laptop for the purpose of data logging and EB gun control. Both systems were controlled using the LabVIEW program installed on the laptop. The USB-1208HS-4AO was used to output a beam deflection signal, which was then amplified to control the beam deflection system, allowing user-defined beam patterns to be drawn on the surface of the button. The USB-2416-4AO was used to log a variety of information including thermocouple data, the operating pressure within the EB gun and furnace chamber and the currents/voltages of the EB gun filament, exciter and electron beam.

4.2.2 Temperature Measurements

The temperature variation within the button and mold was measured during each experiment using three type-C thermocouples located in the button and a type-K thermocouple located

within the mold. The thermocouple locations are shown in Figure 4.4.

(a) TCs After the Experiment

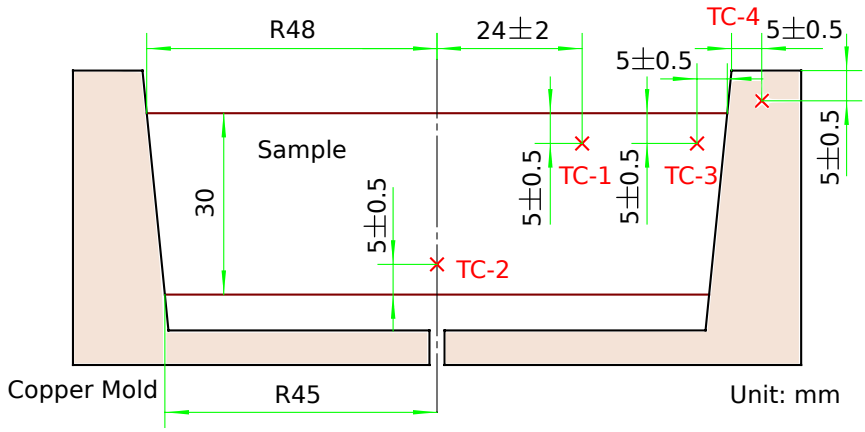

(b) Diagram of TC locations

Figure 4.4: Photo and Schematic Showing the Locations of the Thermocouples

TC-1 was dipped into the liquid pool during the experiment at a user-defined location. For the experimental setup shown in Figure 4.4(a), TC-1 was 24 ± 2 mm away from the center and 5 ± 1 mm below the top surface of the button. TC-2 was embedded on the centerline of the button, 5 ± 0.5 mm above the bottom surface. TC-3 was placed 5 ± 0.5 mm below the top surface and 5 ± 0.5 mm away from the edge of the button adjacent to the mold. The type-C thermocouple wires were sheathed in high purity (over 99.8%) alumina ceramic to minimize exposure of the thermocouple wire to the environment within the furnace chamber. The type-K thermocouple, TC-4, was located in the copper mold 5 ± 0.5 mm away from the mold interface with the button and 5 ± 0.5 mm below the top surface of the mold

and was also sheathed for protection, as shown in Figure 4.4.

In addition to measuring and recording the temperature within the button and mold, four type-T thermocouples were installed separately in the inlets and outlets of the mold and gun water cooling systems. During the experiments, constant temperature differences between the inlets and outlets were considered to be one indicator that the liquid pool had reached steady state.

As type-C thermocouples (W-5% Re/W-26% Re) are not directly supported by the DAQ system drivers, a polynomial was used in the LabVIEW program to convert the millivolt signal measured with the thermocouples to temperature[30]. Details of the conversion are presented in Appendix A.

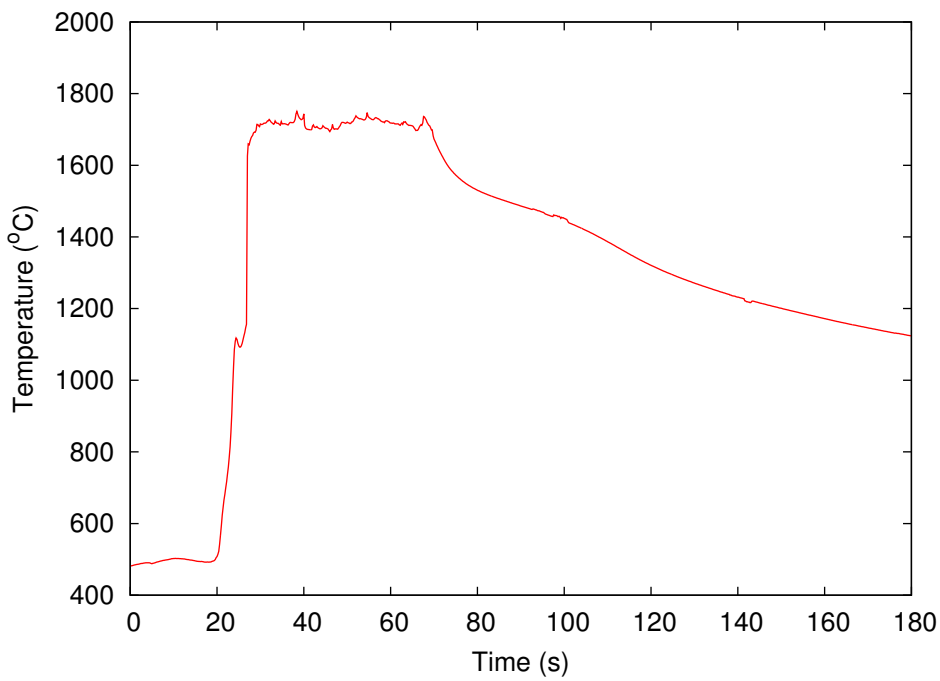

Figure 4.5: Temperature Recorded by TC-1 Thermocouple. EB Power Maintained at 10.0±0.5 kW (Dipping Depth: 5 mm)

Prior to conducting the bulk of the experimental program, several initial experiments were conducted with Ti-6Al-4V to assess the best method of inserting TC-1 into the liquid pool. It was found that a wider beam pattern resulted in less damage to the thermocouple sheathing and that the immersion time needed to be limited to around 20s to avoid both

damage to the sheathing and chemical attack on the thermocouple wire by liquid titanium. Figure 4.5 shows the result obtained for the optimal insertion methodology at an EB power of 10.0±0.5 kW. As can be seen, following an initial rapid rise in temperature associated with insertion of the thermocouple into the liquid, an approximately stable temperature was obtained with an average reading of 1700 ^{o}C for close to 30s, prior to turning the power off and allowing the button to cool. This was in agreement with Suzuki's experiments[13], in which a type-C thermocouple sheathed by a yttria tube (more stable than alumina in molten titanium[2]) was found to survive for about 50 seconds after immersion into a CP titanium melt. As the bulk of the experimental program was undertaken at a higher power of between 11 and 13 kW to increase the pool depth, the exposure time was further limited to only 10s.

4.2.3 Velocity Measurements

During the electron beam melting process, direct velocity measurement is extremely difficult due to the high vacuum, the high temperatures involved and the reactivity of titanium. In Kostov's research, alumina was shown to have some stability in liquid titanium and titanium-aluminum alloys, but was unsuitable for long duration containment[2]. Lee *et al.* measured a peak velocity of 0.19 m/s by observing the movement of alumina particles on the surface of liquid IN718 in an EB furnace[14]. In the current research, alumina particles were charged into a screw feeder and then dropped onto the liquid pool as markers to track fluid velocity at the surface. Particle movement was recorded by a Gigabit Ethernet machine vision camera (GC 1290 with a frame rate of 59 FPS from Allied Vision Technologies) mounted at the top viewport of the furnace. After the experiment, the video was analyzed frame by frame to extract velocity information at the pool surface.

4.3 Button Sample

All samples were cut from forged titanium bar stock and machined into the button shape shown in Figure 4.4. Ti-6Al-4V buttons were used to generate data to verify the model

predictions related to aluminum evaporation and the phenomena that are dependent on concentration gradients – i.e. compositional induced buoyancy and surface tension (Marangoni) driven flows. To help clarify the effect of aluminum evaporation and the associated concentration gradients on the flow pattern and pool profile, additional experiments were conducted with CP titanium, in which compositional effects were not present.

Table 4.2: Chemical Composition of Sample Materials (wt%)

Material	Al	C	Fe	H	N	O	Ti	V	Other
Ti-6Al-4V	6.318	0.0365	0.161	0.0003	0.006	0.183	Balance	4.05	0.11
CP Ti	-	0.08	0.30	0.015	0.03	0.25	Balance	-	0.40

Table 4.2 lists the chemical composition of sample materials. The composition of Ti-6Al-4V in Table 4.2 is taken from the chemical specification of the original ingot. The composition of CP titanium is the equivalent of ASTM Grade 2.

4.4 Experimental Procedure

To mount thermocouples (TC-2 and TC-3) in the button samples, two holes were drilled: one in the edge and the other in the bottom. Another hole was drilled in the copper mold, as shown in Figure 4.4. The size of the holes (3.048 mm in diameter and 5 mm in depth) was slightly bigger than the ceramic sheath used to protect the thermocouples. For the thermocouple that was dipped into the liquid pool (TC-1), the dipping position and depth were setup by adjusting positions of the dipping arm and tested prior to running each experiment. All the thermocouple extension wires inside the chamber were wrapped in ceramic fiber cloth to reduce exposure to radiation.

At the start of each experiment, the vacuum and water-cooling systems were turned on. When the pressure reached below 10^{-4} mbar (10^{-2} Pa) in the furnace chamber and about 10^{-5} mbar in the gun chamber, the power to the EB gun was switched on. The EB power was controlled by its accelerating voltage, which was manually increased by 1.6 kV every 3

minutes from 8 kV to 16 kV. The beam scanning pattern was programed using LabView to draw a circular pattern on the top surface of the sample with a scanning frequency of 80 Hz. The position of the circular pattern was manually adjusted each time after the accelerating voltage was increased to ensure its alignment with the sample's geometrical center.

The combination of the measured temperature variation obtained from the various thermocouples the liquid pool surface area observed through the viewport were used to indicate when the pool had reached steady state after the peak accelerating voltage for a particular experiment was reached. In each case, steady state was found to occur after approximately 3 minutes. Therefore, TC-1 was dipped into the pool 3 minutes after the peak accelerating voltage was reached. After dipping the thermocouple, the beam was left on for another 10 seconds to allow the thermocouple reading to stabilize. The electron beam was then switched off and TC-1 was left in the pool to record the temperature during solidification and cooling of the button.

Table 4.3: Parameters Used in the Electron Beam Button Melting Experiments

Date of Experiment	Aug 08	Oct 11	Dec 07	Dec 08
Sample Material	Ti-6Al-4V	Ti-6Al-4V	Ti-6Al-4V	CP Ti
Vacuum (10^{-3}Pa)[1]	1.5–2.2	1.0–2.1	1.5–2.1	1.1–2.2
Filament Current (A)[2]	16±1	16±1	16±1	16±1
Exciter Voltage (V)	810	830	858	882
Exciter Current (A)	0.5±0.1	0.5±0.1	0.5±0.1	0.5±0.1
Beam Voltage (kV)	16.0±0.5	15.0±0.5	16.0±0.5	16.0±0.5
Beam Current (A)	0.82–0.84	0.72–0.73	0.84–0.85	0.79–0.81
Average EB Power (kW)	13.0	11.0	13.4	12.8
EB Pattern Radius (mm)	3±2	12±2	15±2	15±2
EB Scan Frequency (Hz)	80	80	80	80
Water Flow Rate (L/min)	12.25±0.05	12.25±0.05	12.25±0.05	12.25±0.05
Data Frequency (Hz)[3]	5	5	5	5

[1] Chamber pressure under peak beam power.
[2] Filament voltage changed accordingly.
[3] Data recording frequency on the laptop.

During the development of the experimental technique, 8 button samples with near max-

imum pool diameter were sectioned to examine the pool depth. The pool depth data was used to fine-tune the electron beam parameters such as beam power, beam pattern radius and beam power distribution. Parameters for the experiments with pool depth close to or deeper than 10 mm are reported in Table 4.3. The experiment on Aug 08 was used to measure the surface velocity in the liquid pool. The experiments on Dec 07 and Dec 08 were carried out on Ti-6Al-4V and CP Ti, respectively, with approximately the same beam power and beam pattern radius. The experiment on Oct 11 was conducted using a lower beam power and a smaller beam pattern radius relative to the other two experiments.

4.5 Pool Profile and Concentration Profile

After each experiment, the button was left in the furnace to fully cool overnight before being sectioned by wire Electrical Discharge Machining (EDM). A sectioned sample is shown in Figure 4.6. The sample was cut in half vertically through its center. The sectioned surface was etched after polishing to reveal the liquid pool profile to facilitate comparison with the model predictions. The macroetchant consisted of 15 mL HNO_3, 10 mL HF and 75 mL H_2O.

(a) EB Melted Sample **(b)** Polished Surface

Figure 4.6: Photos of EB Melted Sample and EDM Sectioned Surface

One sample was selected for compositional analysis. In order to fit the sample into the vacuum chamber of a Hitachi S-3000N SEM, a second cut was performed to give an 8 mm thick section as shown in Figure 4.6(b). To avoid potential variation in aluminum

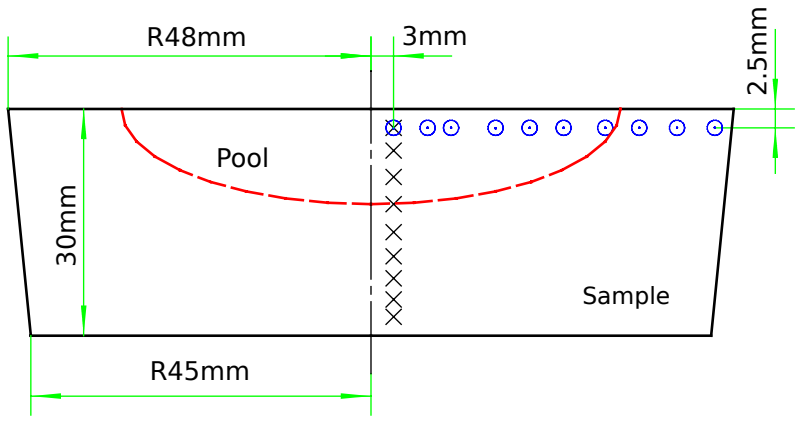

Figure 4.7: Concentration Probing Locations on the Sectioned Surface

concentration caused by etching, the etched sample was re-polished before performing EDX analysis in the SEM. The locations of aluminum concentration evaluation on the sectioned surface are shown in Figure 4.7: chemistry analysis was performed at locations across the top portion of the pool and down the centerline. The locations outside the liquid pool were used to establish the original Al content in the sample.

Chapter 5

Numerical Model

The electron beam refining process exhibits complex, interrelated transport phenomena in the melt. These phenomena must be carefully examined and correctly understood in order to build a numerical model capable of providing meaningful predictions with respect to the thermal, flow and compositional fields.

The model developed in this program represents an extension to the EBBM model reported by Meng[27]. In Meng's work, the influence of thermal buoyancy and thermal Marangoni forces on the temperature and flow fields were studied. In the current work, the evaporation of aluminum has been added allowing compositional buoyancy and Marangoni forces to be included and their influence on the thermal and flow fields assessed.

The possible factors driving fluid flow are identified on a schematic of the EBBM process shown in Figure 5.1. For a given mold and button configuration, the size and shape of the liquid pool is largely dictated by the EB power and the pattern described by the beam on the surface. Generally, the top center region has the highest temperature. The temperature decreases radially along the top surface toward the edge of the button and from the top surface down toward the base of the button. The resulting radial temperature gradient leads to thermally induced Marangoni forces on the top surface of the fluid and the vertical gradient to thermally induced buoyancy forces in the bulk of the liquid. These forces

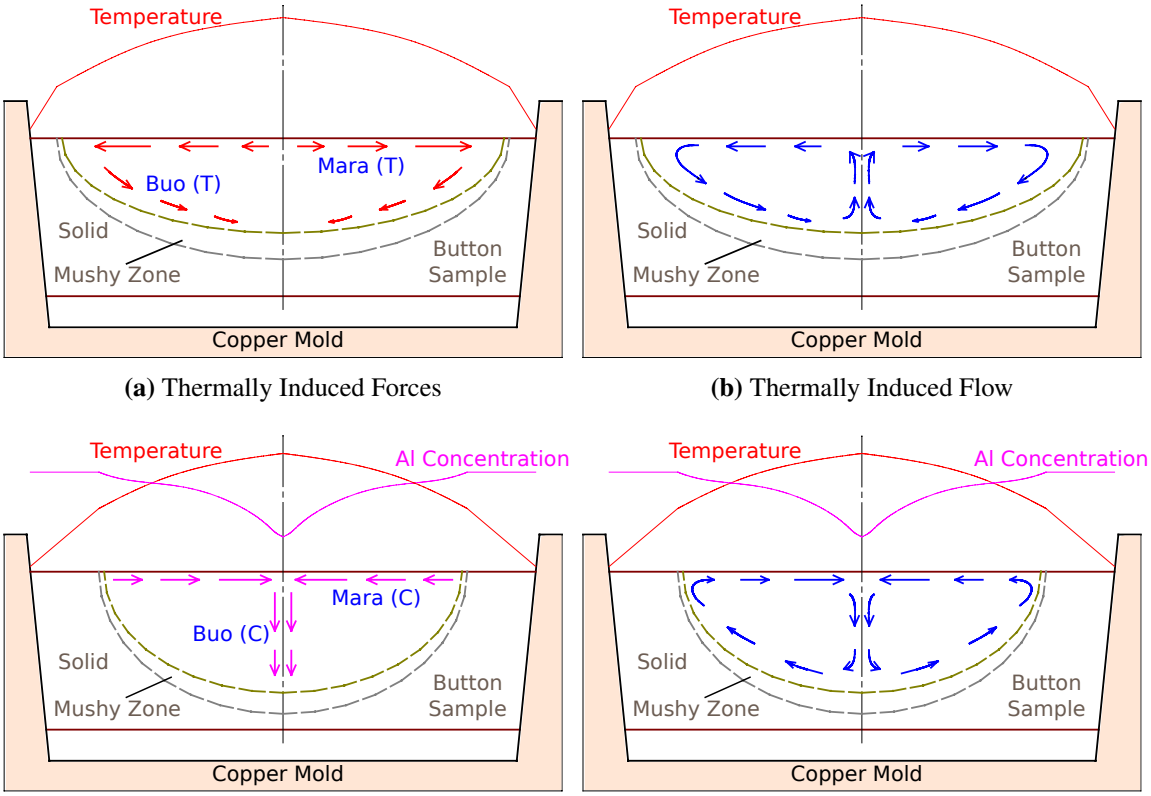

(a) Thermally Induced Forces

(b) Thermally Induced Flow

(c) Compositionally Induced Forces

(d) Compositionally Induced Flow

Figure 5.1: Schematic of Thermally and Compositionally Induced Forces and Flow with Hypothetical Surface Temperature and Concentration Distributions in Electron Beam Button Melting of Ti-6Al-4V

for Ti-6Al-4V are shown schematically in Figure 5.1(a). Consequently, a recirculating flow radially outward along the top surface, down the edge of the liquid pool and upward in the center develops as shown schematically in Figure 5.1(b). Because of the high temperature in the melt and the high vacuum in the furnace, the concentration of aluminum in the liquid at the surface is reduced due to its relatively high vapor pressure. The evaporative loss of aluminum will tend to create concentration gradients within the liquid pool. Generally, the surface will become depleted in aluminum relative to the bulk leading to compositionally driven buoyancy forces. And, in addition, because there is a radial gradient in temperature on the top surface, there will also be a radial gradient in composition and an associated compositionally driven Marangoni force. These forces for Ti-6Al-4V are shown schematically

in Figure 5.1(c). Consequently, a recirculating flow radially inward along the top surface, down the center of the liquid pool and upward along the edge of the liquid pool develops as shown schematically in Figure 5.1(d). As can be seen, due to the specifics of the alloy and the EBBM process, the tendency is that the thermally induced forces oppose the compositionally induced forces.

In addition to the factors identified above, as Ti-6Al-4V is an alloy, a mushy zone exists in the material bounded by the liquidus and solidus isotherms. The semisolid structure within the mushy zone represents a resistance to fluid flow that increases as a function of the fraction solid. As a consequence, this structure tends to reduce velocities in the melt pool.

5.1 Governing Equations

The Navier-Stokes equations listed below were solved numerically using the CFD software package ANSYS CFX to predict the pressure, velocity and temperature fields in the EBBM process. An additional transport equation was also solved to predict the evolution of aluminum concentration[31].

5.1.1 Continuity Equation

The continuity equation, together with the momentum equation, is solved for the pressure and velocity fields:

$$\frac{\partial \rho}{\partial t} + \nabla \cdot (\rho \vec{u}) = 0 \tag{5.1}$$

where ρ is the fluid density (kg/m^3), t is the time (s) and $\vec{u}$ is the fluid velocity (m/s).

5.1.2 Momentum Equation

The momentum equation in vector form is:

$$\frac{\partial (\rho \vec{u})}{\partial t} + \nabla \cdot (\rho \vec{u}\vec{u}) = -\nabla p + \nabla \cdot \tau + S_M \tag{5.2}$$

where p is the pressure (Pa), S_M is the momentum source term ($\mathrm{kg/m^2/s^2}$) and τ is the stress tensor ($\mathrm{kg/m/s^2}$):

$$\tau = \mu \left(\nabla \vec{u} + (\nabla \vec{u})^T - \frac{2}{3} \delta \, \nabla \cdot \vec{u} \right) \tag{5.3}$$

where μ is the dynamic viscosity ($\mathrm{Pa \cdot s}$ or $\mathrm{kg/m/s}$).

The source term (S_M) in the momentum equation is used to account for thermal and compositional buoyancy forces and the resistance to flow within mushy or two phase region as described below.

Compositional and Thermal Buoyancy

The Boussinesq model provided by CFX is suitable for buoyancy flow with density differences driven by small temperature variations. An alternative approach is to employ the full buoyancy model, in which $\rho - \rho_{ref}$ is evaluated directly by the solver when density is defined as a function of temperature or other field variables[31]. Neither of these approaches to incorporate buoyancy in CFX is capable of characterizing buoyancy flow driven by both thermal and compositional variations. Therefore, buoyancy has been included in the model by adding a source term ($S_{M,buoy}$) to the momentum equation with a user-defined subroutine developed in Fortran by Shuster[32]:

$$S_{M,buoy} = (\rho - \rho_{ref}) g \tag{5.4}$$

where ρ ($\mathrm{kg/m^3}$) is a function of temperature and composition, ρ_{ref} ($\mathrm{kg/m^3}$) is the reference density of Ti-6Al-4V at the solidus temperature. In the subroutine where this source term is calculated, the density (ρ) is adjusted based on the aluminum concentration at the previous time step as:

$$\rho = \omega_{Al} \rho_{Al}(T) + (1 - \omega_{Al}) \frac{\rho_{Ti64}(T) - 0.06 \rho_{Al}(T)}{0.94} \tag{5.5}$$

where ω_{Al} is the mass fraction of aluminum, $\rho_{Al}(T)$ is the temperature dependent density of aluminum and $\rho_{Ti64}(T)$ is the temperature dependent density of Ti-6Al-4V. Thus, the density of the material defined in the model is varying with both temperature and aluminum concentration. Both thermal and compositional buoyancy are accounted for by evaluating $\rho - \rho_{ref}$ in the calculation.

Flow Attenuation in the Mushy Zone

Within the mushy zone, the developing microstructure provides increasing resistance to fluid flow as solidification proceeds[33]. This flow attenuation behavior is modeled by including a momentum source term based on Darcy's Law[8, 27, 34]:

$$S_{M,Darcy} = -\frac{\mu}{K}\, u \tag{5.6}$$

where μ is the viscosity (kg/m/s), u is the velocity (m/s) and K is the permeability (m^2) defined by the Carman-Kozeny equation:

$$K = \frac{(1-f_s)^3}{k_c\, s_0^2\, f_s^2} \tag{5.7}$$

where f_s is the fraction solid, s_0 is the solid/ liquid interfacial area per unit volume of solid (m^{-1}) and k_c is the Kozeny constant. In the current model, $k_c s_0^2$ is assumed to have a constant value equals to 1.67×10^{10} m^{-2}[8]. To prevent K from becoming zero in Equation 5.6, the term $1 - f_s$ is limited to 1×10^{-10}.

5.1.3 Energy Equation

The energy equation solved in CFX is formulated based on enthalpy and is equivalent to the following equation:

$$\rho C_p \left(\frac{\partial T}{\partial t} + \vec{u} \cdot \nabla T \right) = \nabla \cdot (k\, \nabla T) \tag{5.8}$$

where C_p is the specific heat capacity (J/kg/K), T is the temperature (K) and k is the thermal conductivity (W/m/K).

5.1.4 Additional Transport Equation

The concentration of aluminum in the domain is defined as an additional variable (ϕ) and calculated by solving the following transport equation:

$$\frac{\partial(\rho\phi)}{\partial t} + \nabla \cdot (\rho\ \vec{u}\ \phi) = \nabla \cdot \left(\rho\ D_\phi\ \nabla\phi\right) \tag{5.9}$$

where ϕ is the conserved quantity per unit mass or the mass fraction (kg/kg) and D_ϕ is the kinematic diffusivity (m^2/s). In the current model, the conserved quantity per unit mass (ϕ) is the mass fraction of aluminum (ω_{Al}) in Ti-6Al-4V.

5.2 Geometry and Mesh

The buttons for the experiments were cut from Ti-6Al-4V and CP titanium bar stock and machined into the shape of a tapered cylinder (refer to Figure 4.4) with a top diameter of 96 mm, a bottom diameter of 90 mm and a height of 30 mm. Assuming a time-averaged circumferentially invariant EB input power distribution and circumferentially invariant button/mold boundary conditions, the computational analysis may be approximated as a 2-D axisymmetric problem. Unfortunately, ANSYS CFX does not allow for 2-D or 2-D axisymmetric analyses to be undertaken. Therefore, to take advantage of the axisymmetric conditions existing in the experiment and to save computational time, the geometry of the sample was reduced to a 5° wedge, as shown in Figure 5.2.

The centerline edge of the wedge shaped geometry is challenging to mesh because the thickness goes to zero. To address this issue, a small portion of the geometry near the centerline has been removed. In the mesh shown in Figure 5.2, the edge of the geometry is cut off by 1 mm from the centerline to avoid numerical instabilities caused by bad mesh

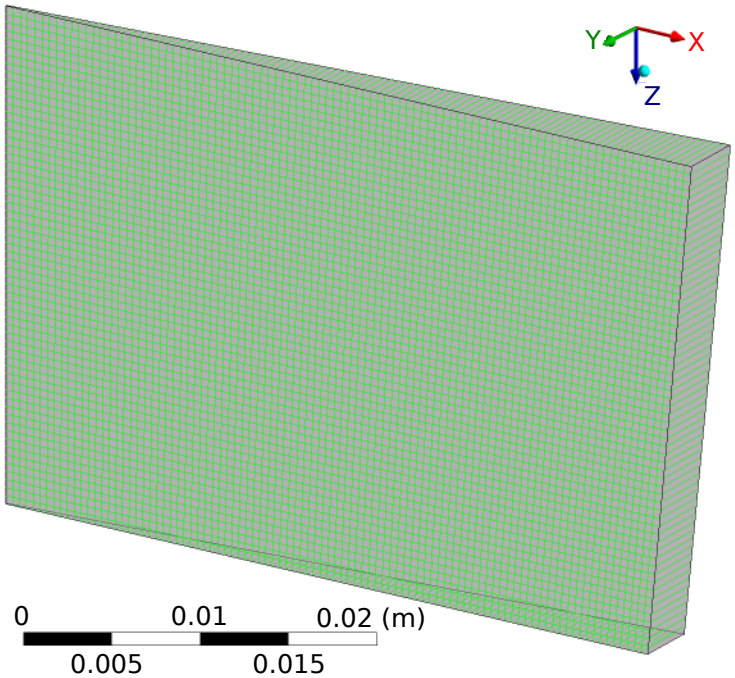

Figure 5.2: 3D View of the Meshed Geometry

quality including high skewness and high aspect ratio. The mesh was generated in Ansys ICEM CFD 12.1 with a mesh size of 0.5 mm. The mesh was generated by first meshing the cross section of the button with 2D quadrilateral elements and then rotating the 2D mesh around the centerline for 5° to create a 3D mesh with one layer of elements in the circumferential direction. The mesh statistics are summarized in Table 5.1.

Table 5.1: Summary of Mesh Statistics

Mesh	Value
Element Type	Hexahedra
Number of Nodes	11834
Number of Elements	5760
Extents: Min x, Max x	1 mm, 48 mm
Extents: Min y, Max y	-4.18 mm, 0 mm
Extents: Min z, Max z	0 mm, 30 mm
Max Edge Length Ratio	8.47
Total Volume	2826.5 mm^3

5.3 Material Properties

Given the objectives of the work, the data needed in the model includes the temperature dependent thermal conductivity, temperature and composition dependent density, temperature dependent specific heat, emissivity, viscosity, and the variation in surface tension with respect to temperature and composition, for both Ti-6Al-4V and CP titanium. In addition, the temperature dependent vapor pressure of aluminum together with the activity coefficient of aluminum is needed for estimation of the evaporation rate of aluminum.

To be able to model the transient heating and cooling of the button, the range of temperatures to be modeled extends from room temperature to above the melting point of both Ti-6Al-4V and CP titanium. As a result, the material may undergo one or both of the solid-state α/β and solid/liquid transformations, depending on its location within the button. The bulk of the material property data for Ti-6Al-4V and CP titanium used in the model are based on the data published by Mills[1]. The application of this data over the entire temperature range required some assumptions to be made within the solid-state transformation temperature range and the melting temperature range of the alloy and in the liquid, as typically the full range of data was not available.

To begin, the solidus and liquidus temperatures for Ti-6Al-4V were taken to be 1595 and 1625 ^{o}C, respectively, from Shyy[23]. The evolution in fraction solid for Ti-6Al-4V within the solidus to liquidus temperature range was obtained from the commercial thermodynamic code Pandat^{TM}[1], which was scaled to agree with the solidus and liquidus temperatures obtained from Shyy. CP titanium was assumed to melt over a 5 ^{o}C temperature range from the melting point of 1668 to 1673 ^{o}C in order to allow use of the equivalent specific heat method (described below). The evolution in fraction α phase within the solid-state α/β transformation was assumed to occur over a 510 ^{o}C temperature range from 494 to 1004 ^{o}C for Ti-6Al-4V and a 10 ^{o}C range from 872 to 882 ^{o}C for CP titanium. The evolution in

[1]Pandat^{TM} is developed for multi-component phase diagram calculation and materials property simulation by CompuTherm LLC, Madison, WI USA

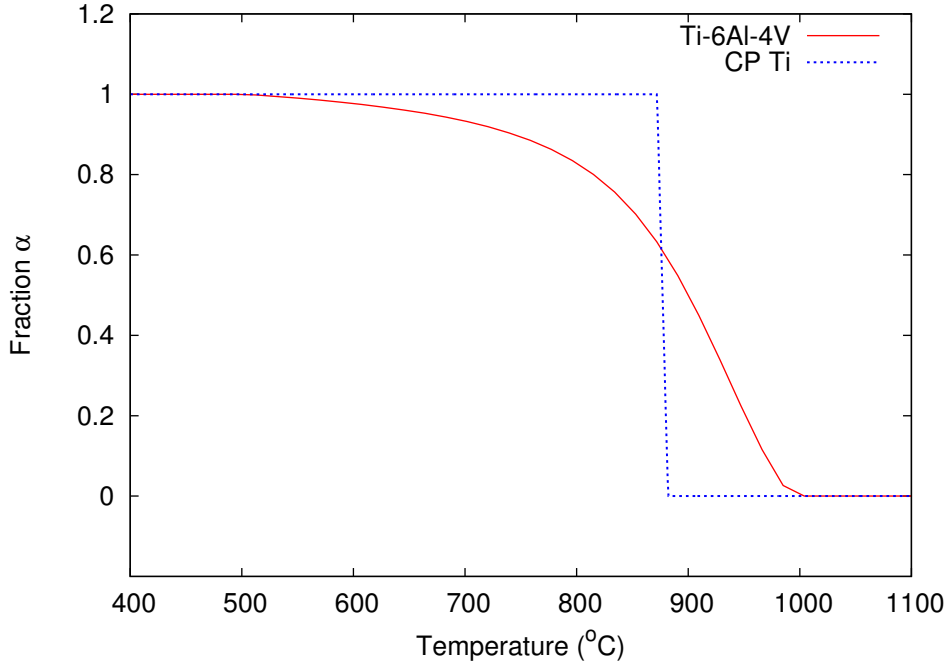

(a) Evolution in Fraction α with Temperature

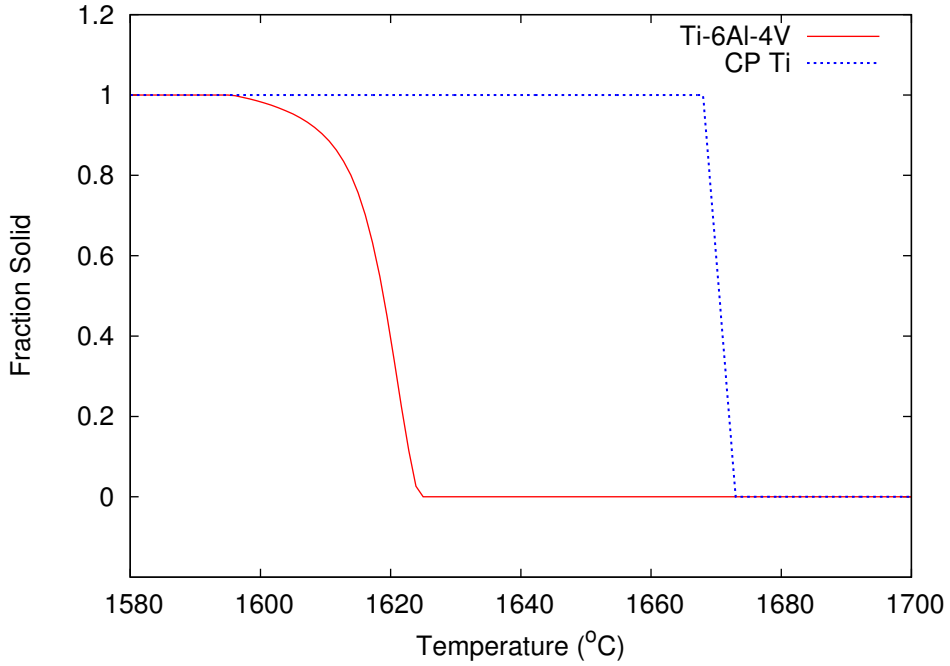

(b) Evolution in Fraction Solid with Temperature

Figure 5.3: Evolution in Fraction α and Fraction Solid for Ti-6Al-4V and CP titanium

fraction fraction α, f_α, and fraction solid, f_s, for the two alloys are shown in Figures 5.3(a) and 5.3(b), respectively.

The variation in density, thermal conductivity, specific heat and viscosity with temperature for Ti-6Al-4V and CP titanium are plotted in Figures 5.4 (a) through (d), respectively.

The modified density data as a function of temperature are plotted in Figure 5.4(a) for Ti-6Al-4V and CP titanium. In general, the density decreases with increasing temperature. Since the volume of the domain in the current model does not change, the mass in the domain is not conserved when the density changes with temperature. By limiting density variations to temperatures above the solidus temperature, where mass feeding can occur to compensate for density changes, errors associated with a lack of mass conservation in the solid can be minimized.

The inaccuracy associated with the fixed volume of the domain has been estimated by running two cases and examining the change in predicted temperature, aluminum content and surface velocity at steady state. In one case, the density variation was limited to temperatures above the solidus temperature and in the other case a constant density was used throughout the entire temperature range. In both cases, the evaporation of aluminum was excluded to eliminate aluminum loss due to evaporation and the associated increase in density. To ensure identical flow drivers in both cases, buoyancy was also excluded. The differences in the highest temperature, the lowest aluminum concentration and the maximum surface velocity predicted in the case with density variations are 0.08%, -3.47% and 0.25%, respectively. Considering the numerical complexities associated with strict mass conservation, which would require a free surface and deformable mesh within the solid, the small differences observed in the two cases run is assumed to justify the adoption of a constant volume domain.

Thermal conductivity as a function of temperature is plotted in Figure 5.4(b). The thermal conductivity is assumed to vary linearly within the solid/liquid phase change temperature range for the two alloys and is held constant for temperatures above the assumed

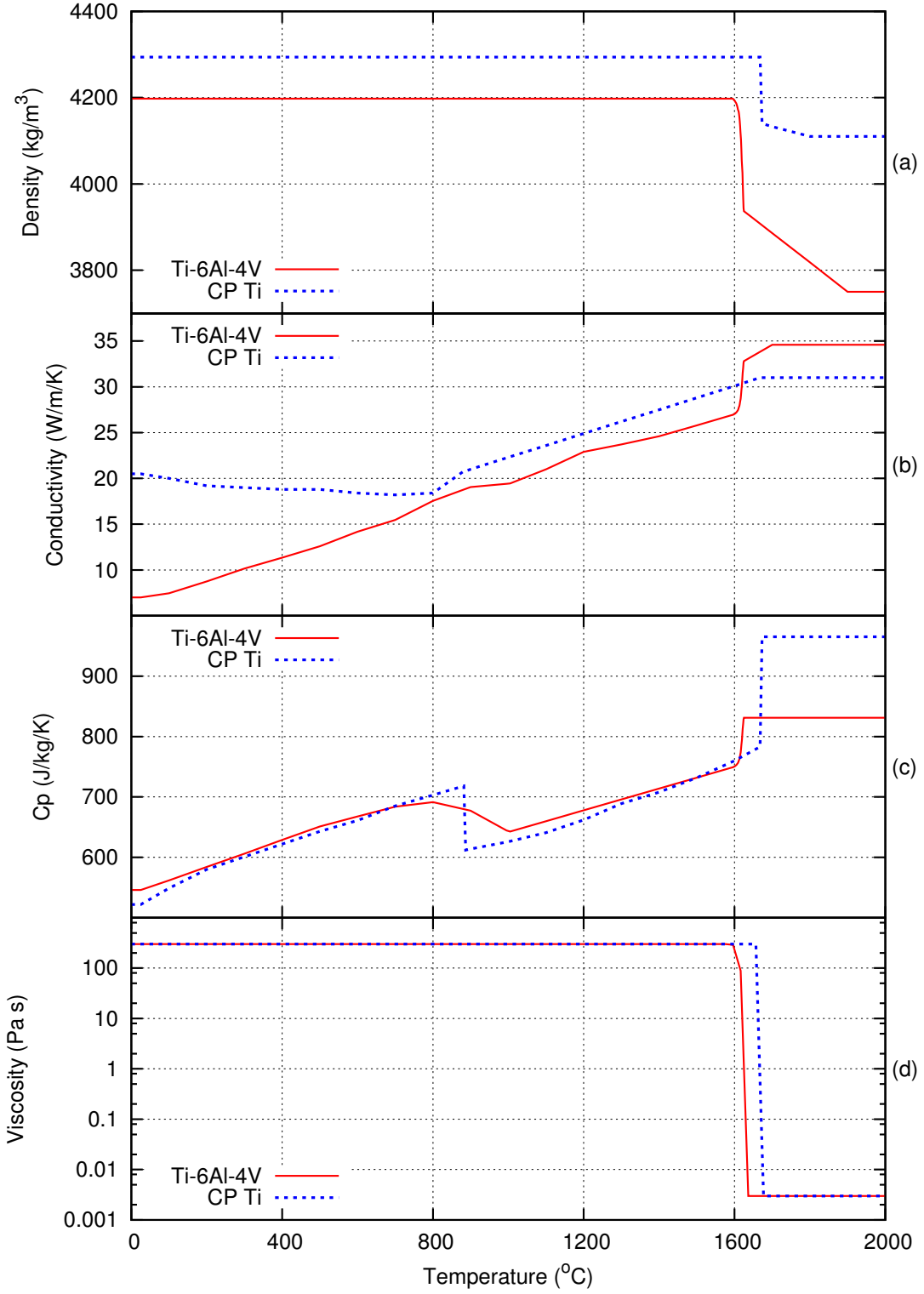

Figure 5.4: Thermophysical Properties for Ti-6Al-4V and CP Titanium[1, 8, 27]

liquidus for the two alloys.

The temperature dependent specific heat used in the model for the two alloys is plotted in Figure 5.4(c). The change in specific heat over the α/β transformation is as presented in the literature. The change over the solid/liquid transformation is assumed to be linear. The release of latent heat during both the solid/liquid and the α/β phase transformations is included in the model using the Effective Specific Heat method[8, 27]. The equation used to calculate the Effective Specific Heat is

$$C_p^E = C_p - L_{s/l}\frac{\mathrm{d}f_s}{\mathrm{d}T} - L_{\alpha/\beta}\frac{\mathrm{d}f_\alpha}{\mathrm{d}T} \tag{5.10}$$

where the specific heat capacity (C_p in J/kg/K) is augmented to account for the evolution of fraction solid (f_s) and fraction of α phase (f_α). $L_{s/l}$ is the latent heat from liquid to solid phase transformation (286 kJ/kg for Ti-6Al-4V and 295 kJ/kg for CP titanium) and $L_{\alpha/\beta}$ is the latent heat from β to α phase transformation (48 kJ/kg for Ti-6Al-4V and 87 kJ/kg for CP titanium)[1]. The calculated effective specific heat (C_p^E in J/kg/K) as a function of temperature for both alloys is shown in Figure 5.5.

The viscosities applied in the model for Ti-6Al-4V and CP titanium are plotted in Figure 5.4(d) as a function of temperature. The limiting fully liquid viscosities are assumed to be the same for the two alloys and are based on the original data reported by Wunderlich[18]. As the entire domain is treated as a liquid, a temperature dependent viscosity is used as one of the two methods to suppress fluid flow in the solid. Hence, the viscosity is ramped from $0.0037 \pm 20\%$ Pa $\cdot$ s at the liquidus of the alloy to 300 Pa $\cdot$ s at the solidus for both alloys. The second method of suppressing fluid flow in the solid is to decrease the permeability appearing in the Darcy source term in the momentum equation (see Equations 5.2, 5.6 and 5.7). Equation 5.6 used the evolution in viscosities over the solidification temperature ranges for the two alloys shown in Figure 5.4(d) and Equation 5.7 used the evolution in fraction solid over the temperature ranges shown in Figure 5.3(b). Together with the large decrease in

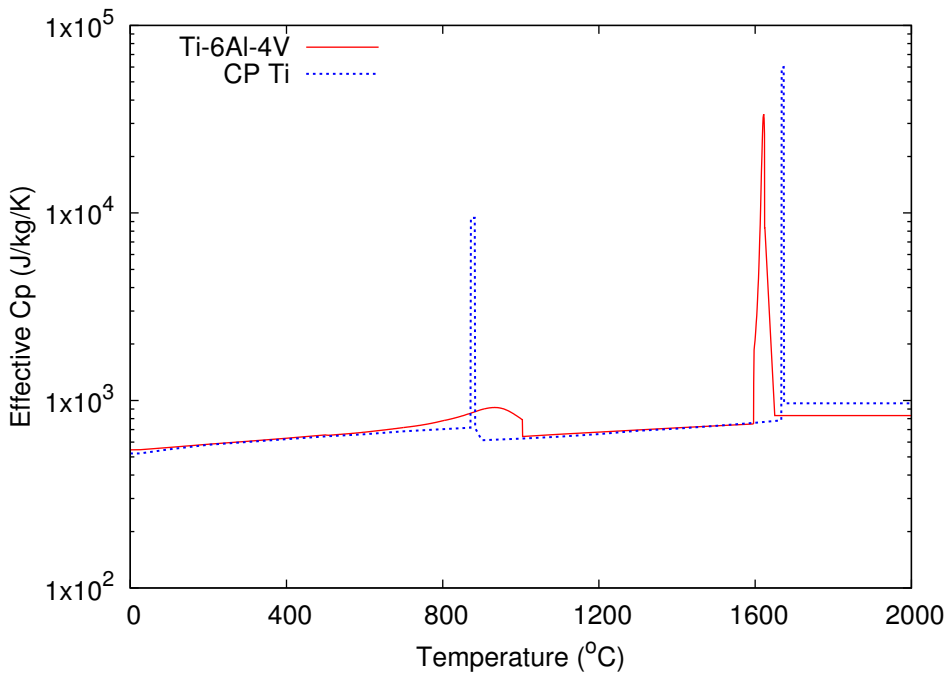

Figure 5.5: Effective Specific Heat of Ti-6Al-4V as a Function of Temperature

permeability, the 5 orders of magnitude increase in viscosity suppresses fluid motion within those portions of the domain below the solidus temperature without causing numerical instabilities.

By extrapolating the tracer impurity diffusion coefficient data for aluminum in α-Ti, the diffusivity of aluminum in Ti-6Al-4V (D_{Al} in $\mathrm{m^2/s}$) was defined in Arrhenius form as:

$$D_{Al} = Ae^{-\frac{Q}{RT}} \tag{5.11}$$

where A (9.7×10^{-9} $\mathrm{m^2/s}$) is the pre-exponential factor, Q (115.1 $\mathrm{kJ/mol}$) is the activation energy, R (8.314 $\mathrm{J/K/mol}$) is the gas constant and T (K) is the temperature[35].

The remaining parameters needed in the model are summarized in Table 5.2 together with the references used. The surface tension coefficients with respect to temperature and composition have been used to calculate the Marangoni force induced by the variations in temperature and aluminum concentration at the surface of the liquid pool. The emissivity has been used to calculate the radiation heat loss from the surfaces of the button sample to

Table 5.2: Model Parameters for Ti-6Al-4V and CP Titanium Used in the Model

Material Property	Symbol	Ti64	CP Ti	Unit	Ref.
Surface Tension Coeff. (T)	$\frac{\partial \gamma}{\partial T}$	-4.5	-1.56	10^{-4} N/m/K	[15, 17, 18]
Surface Tension Coeff. (C)	$\frac{\partial \gamma}{\partial C}$	-0.16	-	N/m	[16]
Emissivity (Liquid Surface)	ε_{liq}	0.4	0.4	-	[36]
Emissivity (Solid Surface)	ε_{sol}	0.6	0.6	-	[36]

the copper mold and the vacuum chamber of the furnace.

5.4 Initial Conditions

At the beginning of a typical simulation with the model, the initial temperature of the domain is set to 200 ^{o}C based on the temperature measured by the thermocouples located at the edge and bottom of the button sample after setting and adjusting beam parameters. The velocity is set to 0 m/s and the initial mass fraction of aluminum is set to 0.06. The pressure calculated in CFX is relative to the specified reference pressure. With the current boundary conditions, the modeling result is not affected by the initial pressure. Both the reference pressure and the initial pressure are set to 0 Pa.

5.5 Boundary Conditions

The boundary conditions applied in the model are summarized in Figure 5.6. The sample is seated in an open-cavity, water-cooled copper mold, as shown in Figure 4.4. While the tapered side surface of the sample is in contact with the mold, there is a 10 mm gap between the bottom of the sample and the bottom of the mold cavity. The specifics of the various boundary conditions are presented in the following sections.

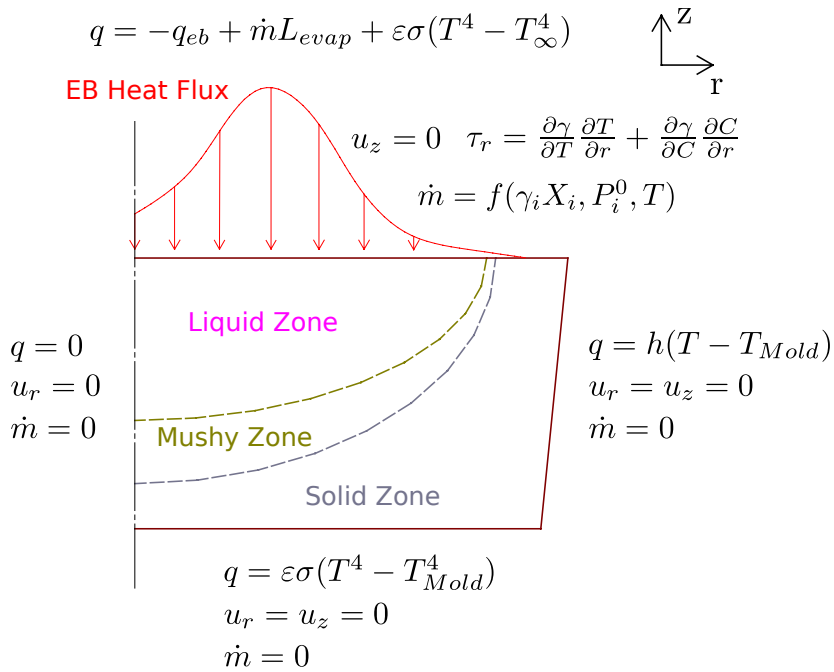

Figure 5.6: Summary of Boundary Conditions

5.5.1 Thermal Boundary Conditions

Electron Beam Heat Flux Distribution

The input heat flux distribution from the EB is assumed to vary in intensity about a point on the surface of the button that can be described by a normal distribution in the form of Equation 5.12. This yields the heat flux at an arbitrary point (x,y) on the sample's surface caused by an electron beam with the spot centered at (x_o, y_o)[5]:

$$q_{eb}(x,y) = \eta_{eb}\, P_{eb}\, \frac{1}{2\pi\sigma^2} e^{-\frac{(x-x_o)^2+(y-y_o)^2}{2\sigma^2}} \tag{5.12}$$

where η_{eb} is an efficiency coefficient accounting for the conversion from kinetic energy of the electrons striking the surface to thermal energy at the beam impingement point. P_{eb} (W) is the total power applied at the electron beam gun, which is the product of the beam current and accelerating voltage.

During the experiments, the electron beam was programed to move in a circle on the

top surface of the sample. The pattern was centered on the sample with a radius of r_o and repeated with a frequency of f (Hz). The heat flux received by an arbitrary point (x,y) at time t becomes:

$$q_{eb}(x,y,t) = \eta_{eb}\, P_{eb}\, \frac{1}{2\pi\sigma^2} e^{-\frac{[x-r_o cos(2\pi ft)]^2+[y-r_o sin(2\pi ft)]^2}{2\sigma^2}} \tag{5.13}$$

With a frequency higher than 10 Hz, the heat flux can be time-averaged without affecting the temperature and velocity fields in the liquid pool[27]. To apply Equation 5.13 in the current model, the heat flux from the electron beam is time-averaged by dividing the pattern evenly into N impingement points where each point has a dwell time of t_i. The total time required to complete the entire pattern is t_N. By adding together the heat flux contributed from each of the N points, the heat flux at an arbitrary point (x,y) is time-averaged to[8]:

$$q_{eb}(x,y) = \eta_{eb}\, P_{eb}\, \frac{1}{2\pi\sigma^2} \sum_{i=1}^{N} \frac{t_i}{t_N}\, e^{-\frac{[x-r_o cos(2\pi i/N)]^2+[y-r_o sin(2\pi i/N)]^2}{2\sigma^2}} \tag{5.14}$$

Heat Loss by Al Evaporation

The heat loss due to aluminum evaporation from the top surface of the liquid pool is calculated by[5, 27, 37]:

$$q_{evap} = \dot{m}_{Al} L_{evap} \tag{5.15}$$

where $\dot{m}_{Al}$ (kg/m^2/s) is the mass flux of evaporated aluminum and L_{evap} (J/kg) is the latent heat of aluminum vaporization (1.39×10^4 kJ/kg[38]). The method used to estimate the mass flux of aluminum is discussed in Section 5.5.3.

Heat Loss by Radiation

Due to the high vacuum environment and the lack of physical contact, convective and conductive heat transfer from the top and bottom surfaces of the button sample is neglected in

the model. Radiation is assumed to be the primary mechanism for the heat loss from the top surface of the button to the furnace chamber and from the bottom surface of the button to the copper mold. The button and the furnace chamber are assumed to behave as gray bodies and the heat loss by radiation is described by[5, 8, 27]:

$$q_{rad} = \varepsilon \sigma_{sb} \left(T^4 - T_\infty^4 \right) \tag{5.16}$$

where ε is the emissivity of the sample surface (refer to Table 5.2), σ_{sb} ($\mathrm{W/m^2/K^4}$) is the Stefan-Boltzmann constant and T (K) is the surface temperature. For the top surface, T_∞ is the temperature of the water-cooled furnace chamber (assumed to be 288 K or 15 ^{o}C) while for the bottom surface, T_∞ is the temperature of the water-cooled copper mold (assumed to be 323 K or 50 ^{o}C).

Heat Loss by Conduction

A temperature dependent heat transfer coefficient h ($\mathrm{W/m^2/K}$) is used to calculate the heat extraction from the side surface of the sample through the copper mold[10, 26].

Figure 5.7 shows the variation of the heat transfer coefficient with temperature for Ti-6Al-4V and CP titanium. The temperature dependent heat transfer coefficient is intended to reflect the increased contact between the button and the mold at elevated temperatures due to thermal expansion of both the button material and the mold and reduced contact at lower temperatures due to the formation of a gap.

$$q = h(T - T_{Mold}) \tag{5.17}$$

In Equation 5.17, T (K) is the temperature of the side surface of the sample and T_{Mold} (K) is the temperature of the mold wall (assumed to be 473 K or 200 ^{o}C).

The variation in the heat transfer coefficient with temperature was determined by fitting the predicted pool profiles and cooling curves to the experimental results. The heat transfer

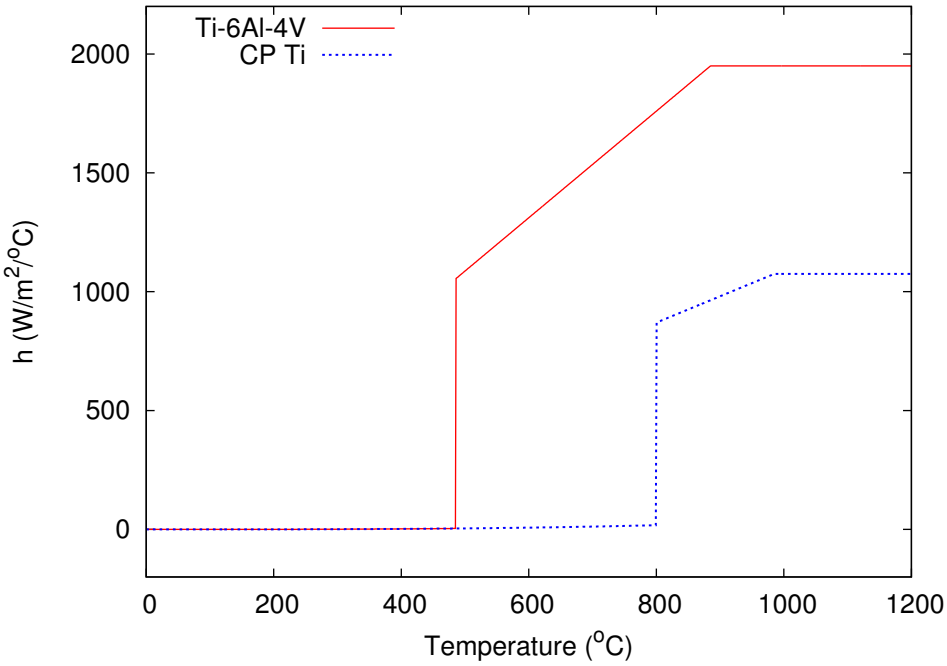

Figure 5.7: Heat Transfer Coefficient as a Function of Temperature

coefficient that provided the best fit of temperature data in the CP titanium case turned out to have a higher gap-forming temperature and lower values at elevated temperatures, as shown in Figure 5.7. The change in heat transfer coefficient is justified by the different thermal behaviors of Ti-6Al-4V and CP titanium observed in the experimental results, i.e. the heat affected region is larger and the measured highest mold temperature is lower in the CP titanium case.

Figure 5.8: Ti-6Al-4V Button (LHS) after the Experiment on Dec 07 and CP Ti Button (RHS) after the Experiment on Dec 08

The change in thermal behavior is attributed to the differences in material property and button/mold interface. Compared with Ti-6Al-4V, CP titanium has a higher liquid/solid phase transformation temperature and lower β/α transition temperature, which could result in different thermal expansion and contraction behavior. Figure 5.8 shows the top and side surfaces of the Ti-6Al-4V and CP titanium buttons after the experiment. Black debris (marked by the red dotted rectangle in the figure), which was originated from the relatively rough surface of the copper mold, was only observed on the side surface of the CP titanium button. The debris at the interface of the CP titanium button and the copper mold could serve as an insulating layer and result in a reduced interfacial heat transfer coefficient.

5.5.2 Momentum Boundary Conditions

Surface Tension Driven Flow

As the electron beam heats the top surface with a relatively concentrated source of energy and aluminum also evaporates from the liquid at this surface in proportion to the temperature, significant temperature and concentration gradients can develop on the surface of the melt. The variations in surface tension caused by these temperature and concentration gradients become driving forces for fluid flow in the liquid pool. To include the effects of surface tension driven flow in the model, a specified shear stress (τ_r in $\mathrm{N/m^2}$) is applied to the top surface[14, 27].

$$\tau_r = \frac{\partial \gamma}{\partial T} \cdot \frac{\partial T}{\partial r} + \frac{\partial \gamma}{\partial C} \cdot \frac{\partial C}{\partial r} \tag{5.18}$$

where γ (N/m) is the surface tension, T (K) is the temperature, C (kg/kg) is the concentration or mass fraction of aluminum. $\frac{\partial \gamma}{\partial T}$ and $\frac{\partial \gamma}{\partial C}$ are the surface tension coefficients with respect to temperature and concentration, respectively (refer to Table 5.2).

The specified shear stress is applied in the model using the Specified Shear boundary condition provided in CFX. In the Specified Shear boundary condition, the velocity components normal to the boundary are set to zero and the user-defined shear stress is applied in

the tangential direction.

No Slip Walls

During the experiments, the liquid pool was contained within solid titanium – i.e. the side and bottom surfaces of the sample remained solid throughout the experiment. In the model, the entire domain is assumed to be a liquid and as previously described, a high viscosity and a Darcy's Law based momentum source term are applied to the material within the solid temperature range to minimize fluid motion. Nonetheless, the side and bottom surfaces of the geometry are set to be No Slip walls in which the velocities of the fluid are zero at the boundaries.

5.5.3 Mass Boundary Conditions

Evaporation of Aluminum

The vapor pressures and evaporation rates for aluminum, titanium and vanadium were calculated by Powell *et al.* in their study of multicomponent evaporation in the electron beam melting of titanium alloys. The results showed that, in the range from 1600 to 2200 ^{o}C, the evaporation rate of aluminum is about three orders of magnitude higher than that of titanium and vanadium[24]. Material properties of Ti-6Al-4V such as density and surface tension coefficient are most sensitive to the evaporative loss of aluminum compared with titanium and vanadium. Therefore, only the evaporation of aluminum has been considered in the current model to reduce complexity in the calculation.

The mass flux of aluminum evaporated from the molten surface of a Ti-6Al-4V sample in a vacuum environment can be calculated with the Langmuir equation, which is given below[10, 39]:

$$\dot{m}_{Al} = \gamma_{Al}\, X_{Al}\, P^0_{Al} \sqrt{\frac{M_{Al}}{2\pi RT}} \tag{5.19}$$

where $\dot{m}_{Al}$ (kg/m^2/s) is the mass flux of alumium, γ_{Al} is the activity coefficient of aluminum,

X_{Al} is the mole fraction of aluminum, P^0_{Al} (Pa) is the vapor pressure of pure aluminum at the temperature T (K), M_{Al} (kg/mol) is the molar mass of aluminum and R (J/mol/K) is the ideal gas constant.

The activity coefficients for the elements in liquid Ti-6Al-4V were summarized by Semiatin and Ivanchenko[40]. They found that the activity coefficient for aluminum is independent of composition but is temperature dependent. In the model, γ_{Al} is assumed to be 0.2 at 1680 °C, 0.5 at 2125 °C and to vary linearly with temperature between these points.

The vapor pressure of aluminum (P^0_{Al} in Pa) may be estimated using the following equation[35]:

$$P^0_{Al} = 133.322 \times 10^{\left(-\frac{A}{T}+B+C\cdot\log T+10^{-3}DT\right)} \tag{5.20}$$

where T (K) is the temperature. The values of the constants A, B, C and D are listed in Table 5.3.

Table 5.3: Constants for Calculating Saturated Vapor Pressure of Al[35]

Element	A	B	C	D	Temperature Range (K)
Al	16450	12.36	-1.023	0	1200 – 2800

The mole fraction of aluminum (X_{Al}) is simplified to be a function of its mass fraction (ω_{Al}) by assuming there is no evaporative loss of titanium or vanadium during the melting process ($\omega_{Ti}/\omega_V = 0.9/0.04$ and $\omega_{Al}+\omega_{Ti}+\omega_V = 1$).

$$X_{Al} = \frac{\omega_{Al}/M_{Al}}{\omega_{Al}/M_{Al}+\omega_{Ti}/M_{Ti}+\omega_V/M_V} \tag{5.21}$$

where M_{Al}, M_{Ti} and M_V are the molar masses of aluminum, titanium and vanadium, respectively. Thus,

$$X_{Al} = \frac{\omega_{Al}}{0.4389\omega_{Al}+0.5611} \tag{5.22}$$

Along the side and bottom surfaces, the button remains solid throughout the melting and

solidification process. Thus, a default zero mass flux condition exists on these two surfaces.

5.5.4 Symmetry Planes

The symmetry boundary condition is applied to both of the vertical planes in the domain. The velocity component normal to the Symmetry Plane is set to zero. The gradients of scalar variables including mass fraction, pressure and temperature normal to the Symmetry Plane are also set to zero.

5.6 Basic Model Implementation Verification

The ability of ANSYS CFX to model fluid flow during casting and solidification processes have been verified by various authors[8, 27, 34]. In this work, the predictions of simple 1-D transient models considering heat conduction and mass diffusion were compared with analytical solutions. Using this approach, the heat and mass transfer formulations in CFX were tested and the ability to correctly implement models involving these phenomena was assessed.

5.6.1 1-D Transient Heat Conduction Problem

The first problem used for model verification was the prediction of temperature in a semi-infinite solid starting at a uniform temperature T_i. At time $t = 0$, the surface of the solid at $x = 0$ is exposed to a convective boundary condition with a heat transfer coefficient, h. Assuming the fluid is at a constant temperature, T_∞, the analytical solution to this problem can be expressed as[41]:

$$\frac{T(x,t) - T_i}{T_\infty - T_i} = \text{erfc}\left(\frac{x}{2\sqrt{\alpha t}}\right) - \exp\left(\frac{hx}{k} + \frac{h^2 \alpha t}{k^2}\right)\left[\text{erfc}\left(\frac{x}{2\sqrt{\alpha t}} + \frac{h\sqrt{\alpha t}}{k}\right)\right] \tag{5.23}$$

where x is the distance from the surface of the solid, t is the time, $T(x,t)$ is the temperature at location x and time t, α is the thermal diffusivity and k is the thermal conductivity.

Table 5.4: Model Parameters Used in Heat Conduction Problem

Model Parameter	Symbol	Value	Unit
Conductivity	k	163	W/m/K
Density	ρ	2702	kg/m^3
Specific Heat	C_p	903	J/kg/K
Thermal Diffusivity	α	9.71×10^{-5}	m^2/s
Initial Temperature	T_i	1000	K
Fluid Temperature	T_∞	298	K
Heat Transfer Coeff.	h	800	W/m^2/K

Since ANSYS CFX requires a 3-D geometry, a rectangular solid domain of 0.1 m $\times$ 0.001 m $\times$ 0.001 m was defined and meshed with 0.001 m cubic elements. A heat transfer coefficient (h) was applied to one end of the domain (x = 0). The boundary at x = 0.1 m is specified as an adiabatic wall. The other four boundaries of the domain are defined as Symmetry Planes. The model parameters used in this analysis are summarized in Table 5.4.

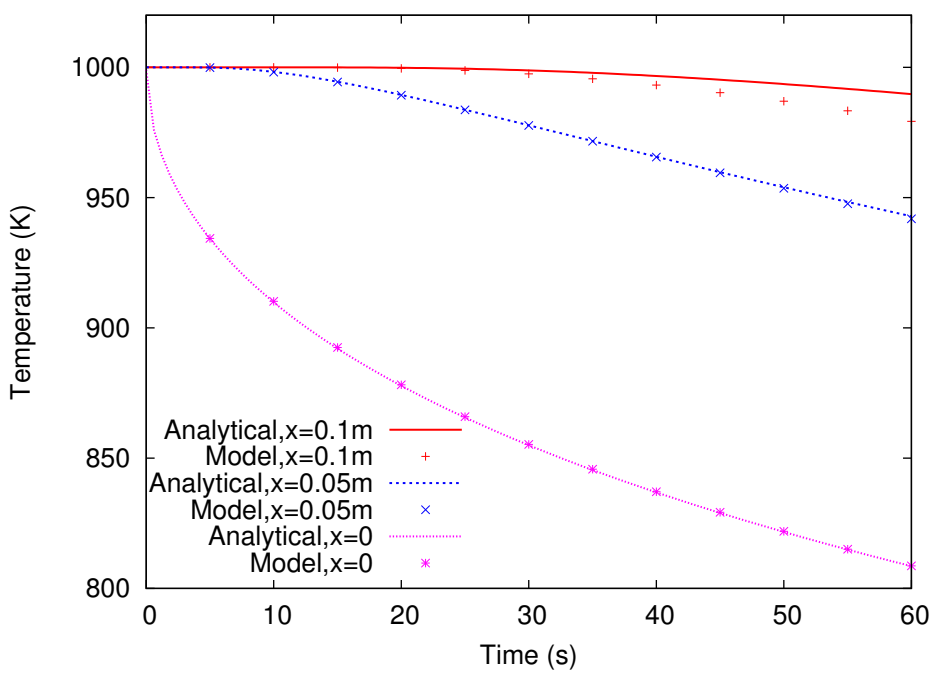

Figure 5.9: Cooling Curves of Numerical and Analytical Solutions

The model was used to predict the temperature evolution in the solid. The results are

plotted and compared with the analytical solution in Figure 5.9. The curves are plotted at three locations in the domain: the surface in direct contact with fluid ($x = 0$), the mid-point of the domain ($x = 0.05$ m) and the other end of the domain ($x = 0.1$ m). The predicted cooling curves are in close agreement with the analytical solution at all three locations before $t = 30$ s. At $t = 30$ s, the temperature at $x = 0.1$ m begins to decrease. Since a finite geometry was used in the model to approximate this semi-infinite problem, the results for times greater than approximately 30 s, the point where the temperature at 0.1 m begins to change from the initial condition, should be ignored as the numerical domain ceases to behave as a semi-infinite domain.

5.6.2 1-D Transient Diffusion Problem

The one-dimensional diffusion problem for a diffusion couple with infinite length was used to test the mass transfer formulation in CFX. The governing equation and the initial condition are given as:

$$\frac{\partial C}{\partial t} = D\frac{\partial^2 C}{\partial x^2}, \qquad C(x,t_0) = \begin{cases} C_0 & \text{if } x \leq 0.05 \text{ m} , \\ 0 & \text{if } x > 0.05 \text{ m} . \end{cases} \tag{5.24}$$

where C is the concentration (kg/kg), D is the diffusivity (m^2/s) and C_0 is the initial concentration. The analytical solution to this problem is[42]:

$$C(x,t) = \frac{C_0}{2}\left(1 - \mathrm{erf}\left(\frac{x - 0.05}{\sqrt{4Dt}}\right)\right) \tag{5.25}$$

A rectangular geometry of 0.1 m $\times$ 0.001 m $\times$ 0.001 m was defined and meshed with 0.001 m cubic elements for this analysis. Zero Mass Flux boundary condition is applied to the two faces that are normal to the side with the longest dimension. The other four faces that are parallel to the lengthwise direction are defined as Symmetry Planes. The model parameters used to solve this transient diffusion problem are summarized in Table 5.5.

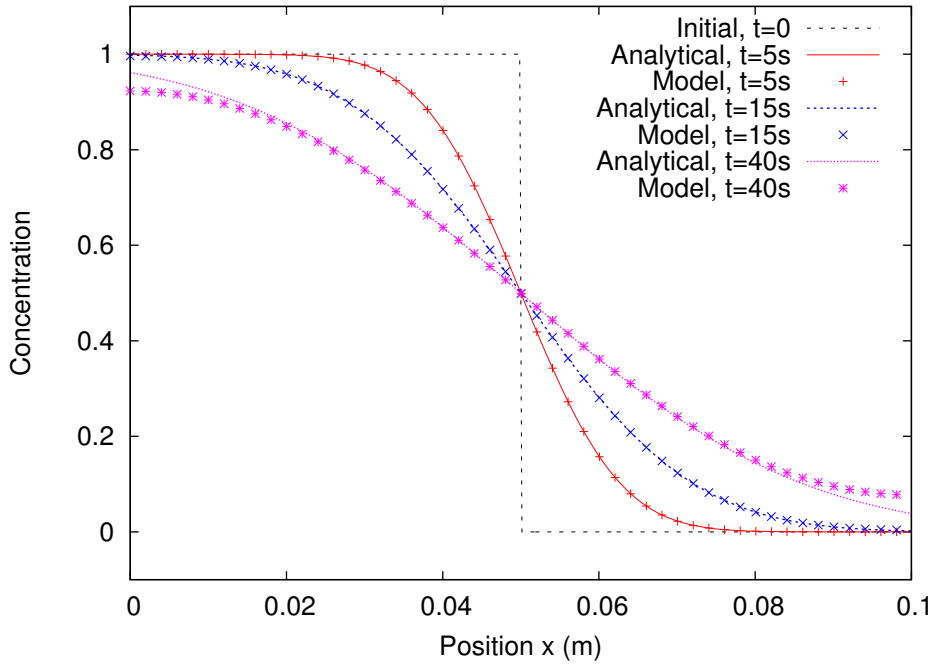

Figure 5.10: Concentration Profiles of Numerical and Analytical Solutions

Table 5.5: Model Parameters Used in Transient Diffusion Problem

Model Parameter	Symbol	Value	Unit
Diffusivity	D	1×10^{-5}	m^2/s
Initial Concentration	C_0	1	kg/kg

The model was used to predict the composition across the diffusion couple with time. Figure 5.10 compares the concentration profiles predicted by the model with those calculated by the analytical solution at three different times: 5s, 15s and 40s. The numerical and analytical solutions exhibit excellent agreement for the 5s and 15s conditions. These times are before the mass diffusion reaches the boundary of the finite domain in the model which has caused the agreement at 40s to deteriorate. The infinite domain cannot be fully represented by the numerical domain once the mass diffusion reaches the boundary of the finite numerical domain.

Chapter 6

Results and Discussion

In this chapter, the predictions made with the model described in Chapter 5 have been compared with the results of the lab-scale Electron Beam Button Melting experiments and where appropriate some of the boundary conditions have been tuned to align the model predictions with the measurements. The model has then been used to study the flow conditions identified in the melting process. Finally, a sensitivity analysis has been conducted to assess the parameters that affect the temperature and velocity fields in the button.

6.1 Experimental and Modeling Results

The model was applied to predict the temperature field, concentration field with respect to the mass fraction of aluminum and flow field in the button samples. Specifically, the variation in temperature with time at the locations of the thermocouples, the liquid pool profile, concentration profile and surface velocity were compared with the appropriate results obtained from the experiments.

6.1.1 Temperature Results

The predicted variations in temperature with time at the positions within the domain corresponding to the locations of the thermocouples are compared with the thermocouple data in

Figure 6.1 through Figure 6.3. Figure 6.1 corresponds to the data obtained from the experiment conducted on October 11th, Figure 6.2 on December 7th and Figure 6.3 on December 8th (refer to Table 4.3). The lines represent the predicted data and the symbols, the experimentally obtained data. Note that the symbols have been plotted at 0.2 Hz for clarity, even though the experimental data was logged at 5 Hz. The locations of the thermocouples in the button sample are presented in Figure 4.4(b). Note only the cooling portion of the experiments is compared as it allows validation of the basic boundary conditions associated with describing the heat losses from the domain – e.g. there is no power input from the electron beam complicating the comparison.

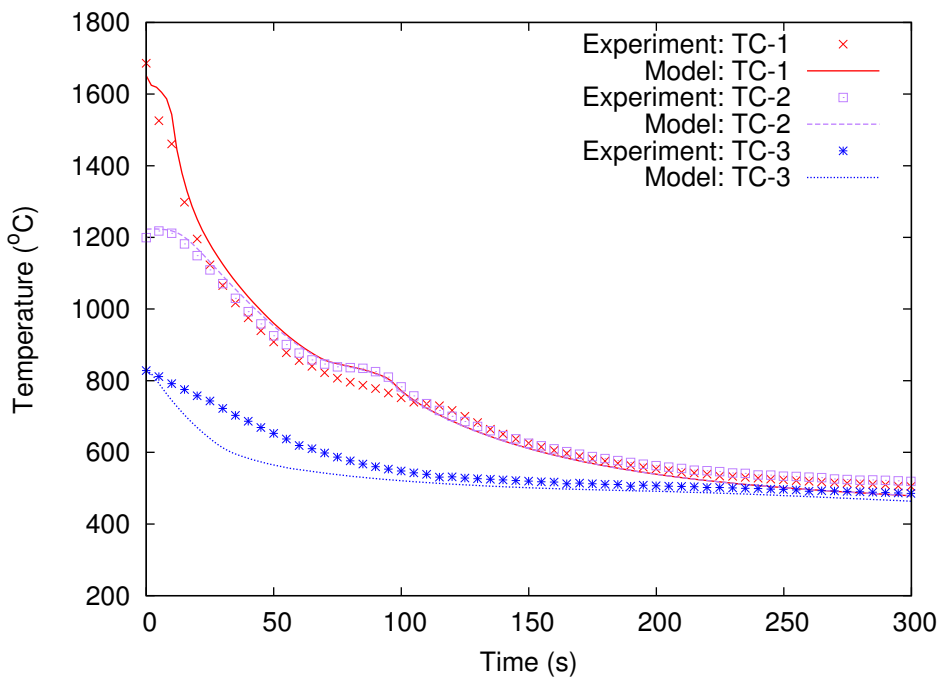

Figure 6.1: Temperature Variations at Three Locations in a EB Button Melting Sample in the Modeling (Lines) and Experimental (Symbols) Results. Experiment was conducted on Ti-6Al-4V with beam power of 11 kW (Oct 11).

Figure 6.1 shows the comparison between the predicted and the measured temperature evolution for the experiment conducted on October 11th on Ti-6Al-4V. As a reminder, TC-1 was located within the liquid pool near the center, TC-2 was embedded in the center near the bottom of the button and TC-3 was located on the top corner near the mold. Overall,

the results show good agreement between the model predictions and measurements during cooling with the EB power off. The effect of the release of latent heat during liquid/solid transformation can be seen in the model predictions for TC-1, but not in the measured data at the resolution plotted. In contrast, the effect of the release of latent heat associated with β/α phase transformations can be seen in both predicted and measured cooling curves for TC-1 and TC-2. The largest discrepancy between the measurements and predictions occurs for TC-3 during the first 100 s. The error probably relates to an underestimation of mold temperature applied in the model to describe heat transfer from the base of the button.

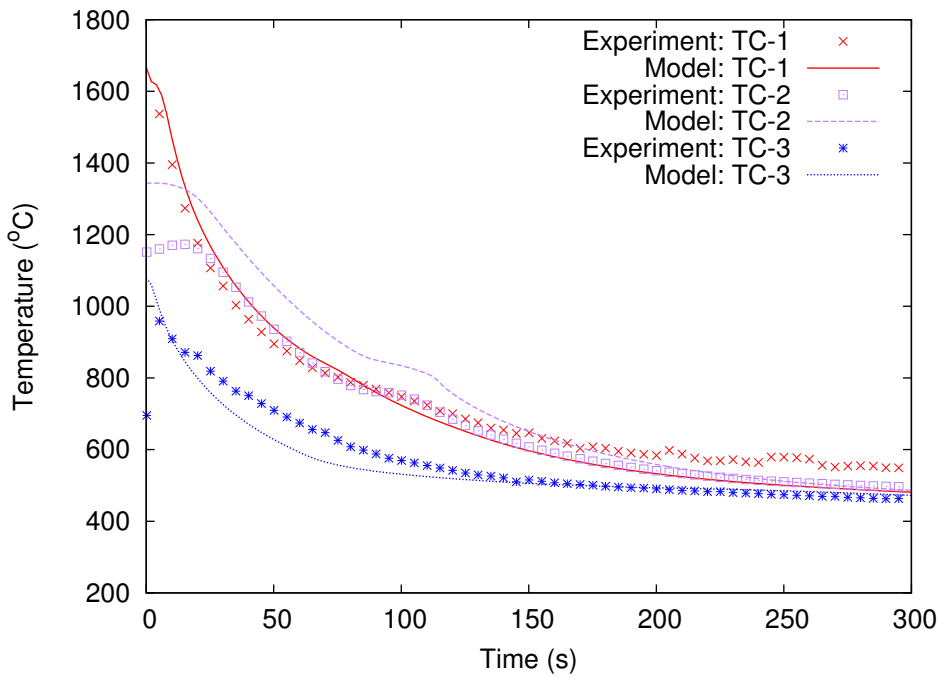

Figure 6.2: Temperature Variations at Three Locations in a EB Button Melting Sample in the Modeling (Lines) and Experimental (Symbols) Results. Experiment was conducted on Ti-6Al-4V with beam power of 13.4 kW (Dec 07).

Figure 6.2 shows the comparison of predicted and measured temperatures for the experiment on December 7th, conducted on Ti-6Al-4V using a slightly higher beam power. In this plot, it can be seen that the predicted cooling curves for TC-1 and TC-3 generally fit the experimental data well, whereas the predictions for TC-2 do not. In particular, during the first 150 to 200 s of the simulation the model predictions for the temperature at the location

of TC-2 are well above the measured temperatures. On closer inspection, it is apparent that the temperatures recorded for TC-2 for the December 7th experiment are lower than the temperatures measured at the same location in both the October 11th and December 8th experiments shown in Figures 6.1 and 6.3, respectively, despite having the highest power input of the three experiments. This suggests that there may have been poor contact between the thermocouple and the button sample leading to an erroneously low measurement.

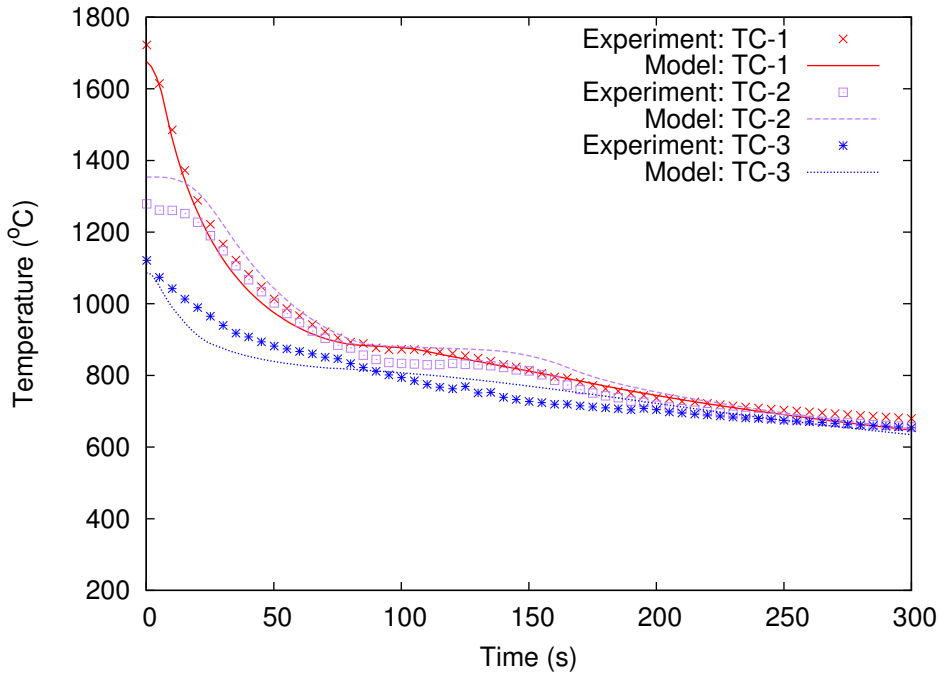

Figure 6.3: Temperature Variations at Three Locations in a EB Button Melting Sample in the Modeling (Lines) and Experimental (Symbols) Results. Experiment was conducted on CP Ti with beam power of 12.8 kW (Dec 08).

Figure 6.3 shows the predicted and measured temperatures for the experiment on CP titanium. The predicted cooling curves are generally in good agreement with the experimental data with the exception of the under prediction of temperature at the location of TC-3 during the first approximately 100 s, which was also observed in the predictions for the October 11th experiment and was attributed to an under estimation of the mold temperature adjacent to the bottom of the button.

6.1.2 Pool Profile and Alpha/ Beta Transition

The results of the pool profile comparisons are shown in Figure 6.4 through Figure 6.6 for the October 11th, December 7th and December 8th experiments, respectively. Etched cross sections of the button samples following each of the three melting experiments are shown on the left-hand-side of each figure together with an image of the predicted temperature contours in the button just prior to the beam being shut off on the right-hand-side. In the two Ti-6Al-4V samples, October 11th and December 7th, the liquid pool profile can be easily identified in the etched sample by the change in grain size from large grains in the liquid pool to smaller grains outside the liquid pool. Note also the abrupt change in grain size from the ultra fine, indicative of the wrought bar stock, to the coarser grain size in the material that remained solid throughout the test. Yang *et al.* used the region that transitioned into the β phase (and the associated increase in grain size) as the α/β transition isotherm and to identify the Heat Affected Zone (HAZ) while modeling Gas Tungsten Arc (GTA) welding of titanium[43]. In the CP titanium sample (December 8th), the change in grain size associated with the liquid/ solid and α/β transformations are less obvious. Close inspection yields a faint line that may be used for demarcation of the liquid/ solid transformation.

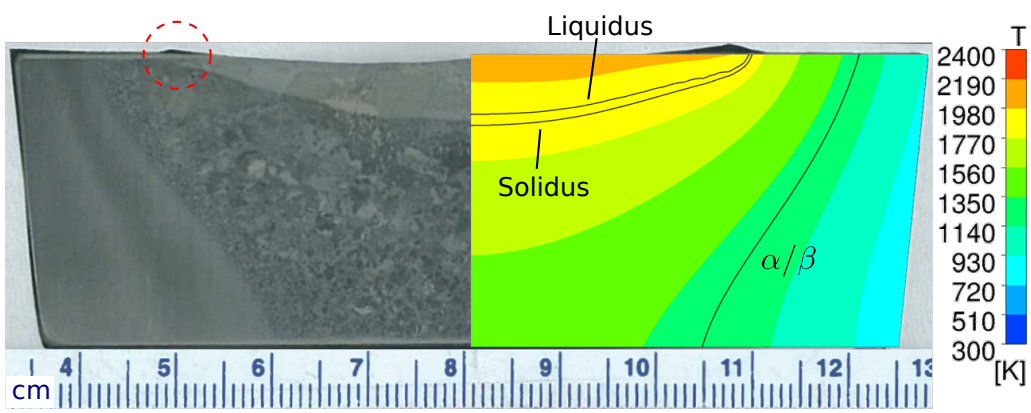

Figure 6.4: Etched Ti-6Al-4V Sample Section (LHS Image) and Predicted Temperature Distribution (RHS Image) (Beam Pattern Radius: 12 mm; Beam Power: 11.0 kW. Oct 11)

The three black lines in the RHS images correspond to the liquidus, solidus and α/β

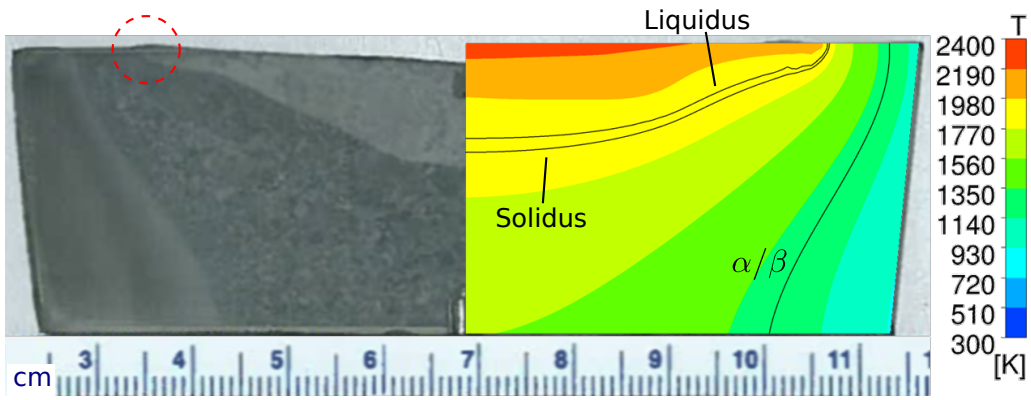

Figure 6.5: Etched Ti-6Al-4V Sample Section (LHS Image) and Predicted Temperature Distribution (RHS Image) (Beam Pattern Radius: 15 mm; Beam Power: 13.4 kW. Dec 07)

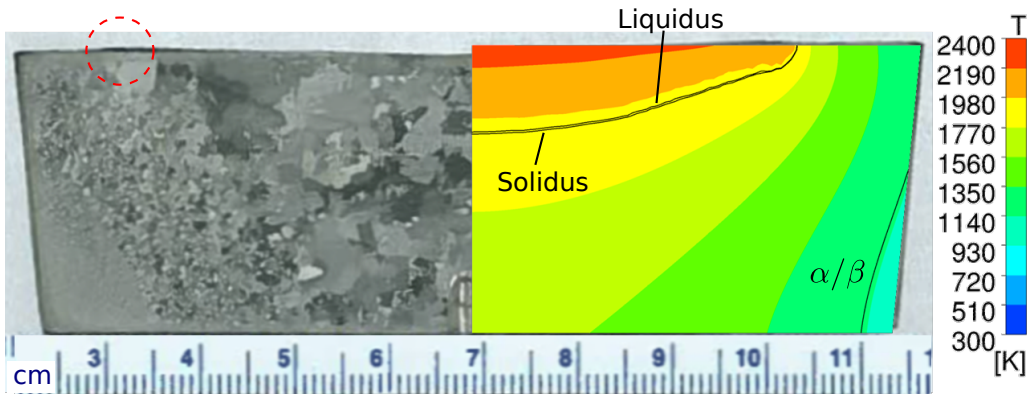

Figure 6.6: Etched CP Ti Sample Section (LHS Image) and Predicted Temperature Distribution (RHS Image) (Beam Pattern Radius: 15 mm; Beam Power: 12.8 kW. Dec 08)

transition isotherms predicted by the model. As can be seen there is relatively good agreement observed based on the shapes and positions of the liquid pools and β regions, as demarked by the microstructural changes, in all three samples. Note the significant loss in mass in the liquid pool (reduction in the height of the top surface where liquid at the center of the sample) present in the Ti-6Al-4V samples (October 11th and December 7th samples), which is primarily associated with the evaporation of aluminum. A secondary contributor to the loss in surface height can be observed at the outer radii of the liquid pool marked in each image with a red dashed circle. Here it would appear that at the beginning of each experiment, prior to substantial evaporation, the thermal expansion in the liquid combined

with surface tension forces has pushed the surface liquid up onto the adjacent solid, where it has solidified leading to a small ridge around the circumference of the liquid pool. Note also some loss in height observed in the CP titanium sample (December 8th) due to evaporation of titanium. In the case of CP titanium, the amount is less due to its lower vapor pressure.

Table 6.1: Summary of Measured and Predicted Pool Depths and Radii

Date of Experiment	Pool Depth D (mm)	Predicted D (mm)	ΔD (%)	Pool Radius R (mm)	Predicted R (mm)	ΔR (%)
Oct 11	5.8	5.7	-1.72	30.5	28.6	-6.23
Dec 07	10.5	9.9	-5.71	35.7	38.2	7.00
Dec 08	8.2	8.8	7.32	36.9	35.4	-4.07

The "Goodness of Fit" for the liquid pool profiles have been assessed by comparing the measured and predicted pool depths, at the center of the samples, and the measured and predicted pool radii. The results are summarized in Table 6.1. Generally, there is agreement to within less than $\pm 8\%$. There are several potential reasons for the errors observed. Firstly, the model adopts a fixed domain analysis (the geometry of the domain remains constant throughout the analysis) and hence is not able to account for the reduction in height of the samples where liquid is lost due to alloy evaporation and solidification shrinkage. The effect of this can be seen by the fact that the model generally under predicts the pool depth for the Ti-6Al-4V experiments. Secondly, control of the beam pattern was difficult and required an adjustment to be made after each increment in power during heat up. Consequently, the center of the beam pattern did not generally coincide with the center of the button, leading to non-symmetric pool profiles, which contributed to error observed in the predicted radii.

6.1.3 Concentration Profile

Figures 6.7(a) and 6.7(b) show comparisons between the predicted and measured aluminum concentration profiles down the centerline and across the top surface along lines approximately bisecting the sample from December 7th experiment, respectively. The predicted

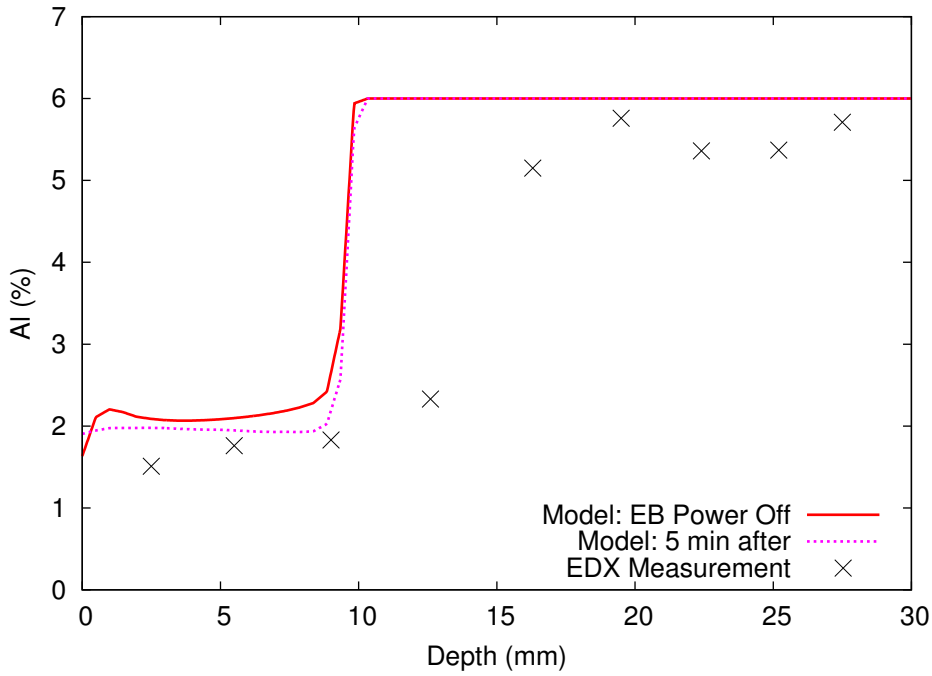

(a) Down the Centerline

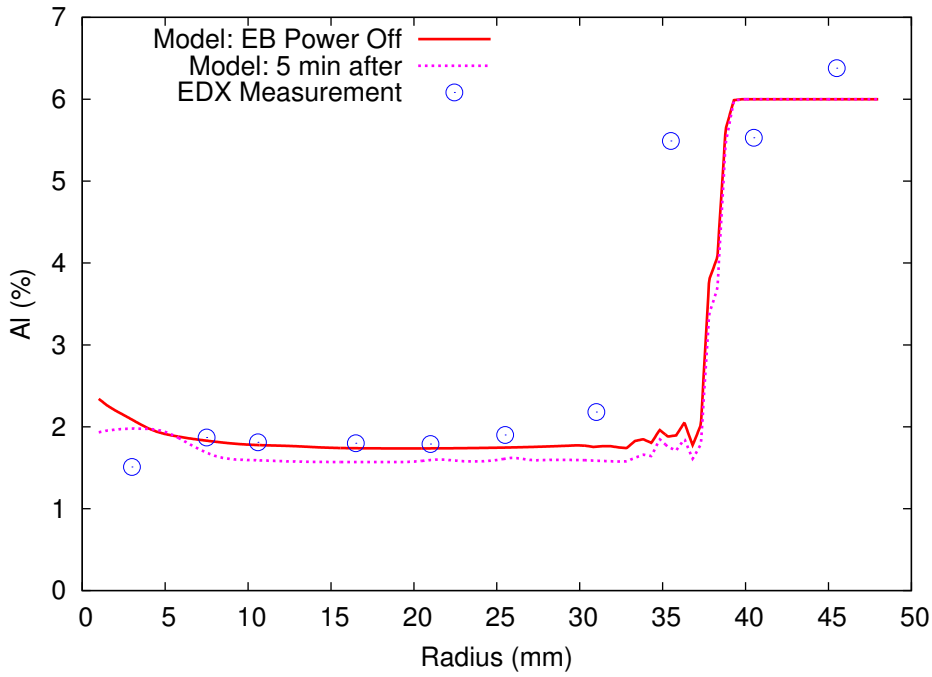

(b) Across the Top Surface

Figure 6.7: Comparison of Predicted and Measured Concentration Profiles in a Ti-6Al-4V Button (Beam Pattern Radius: 15 mm; Beam Power: 13.4 kW. Dec 07)

concentration profiles are plotted at two times: the first, is output from the model when the electron beam is shut off; and the second, 5 minutes after the electron beam is shut off. The results for the second case show the effect of fluid flow on the aluminum concentration distribution during the cooling process, which is generally small.

Turning first to the predicted aluminum concentration down the centerline of the button, Figure 6.7(a), the results show good agreement in the material less than 10 mm in depth and greater than 20 mm in depth. The poor agreement between 10 and 20 mm can be attributed to the under predicted liquid pool depth and the misalignment between the center of the liquid pool and the geometrical center of the button sample. In Figure 6.7(b), the agreement between the predicted and experimental results is also good, apart from in the region where the boundary of the liquid pool resides. This reflects the error in the ability of the model to correctly predict the liquid pool radius. In summary, the overall rate of mass loss of aluminum appears to be correct indicating that Langmuir equation is accurate in quantifying the rate of aluminum loss as implemented in the model. Both of these results agree with Isawa's conclusion that the aluminum concentration is almost homogeneous in the melt pool during the EB melting process[4].

6.1.4 Surface Velocity

Surface velocity measurements were performed by analyzing the recorded video of alumina particles moving on the surface of the liquid pool. When the nominal circular beam pattern was employed, the power to the EB gun cut out immediately after alumina particles were dropped on the sample. However, when the pattern of the electron beam was adjusted to be a small circle in the center of the button sample, the electron beam was stable enough to perform the experiment. The reason why the power to the EB gun cut out when alumina particles were added was undetermined despite repeated attempts to understand this phenomenon. As a result, velocity measurements were limited to an experiment with a highly centered electron beam pattern.

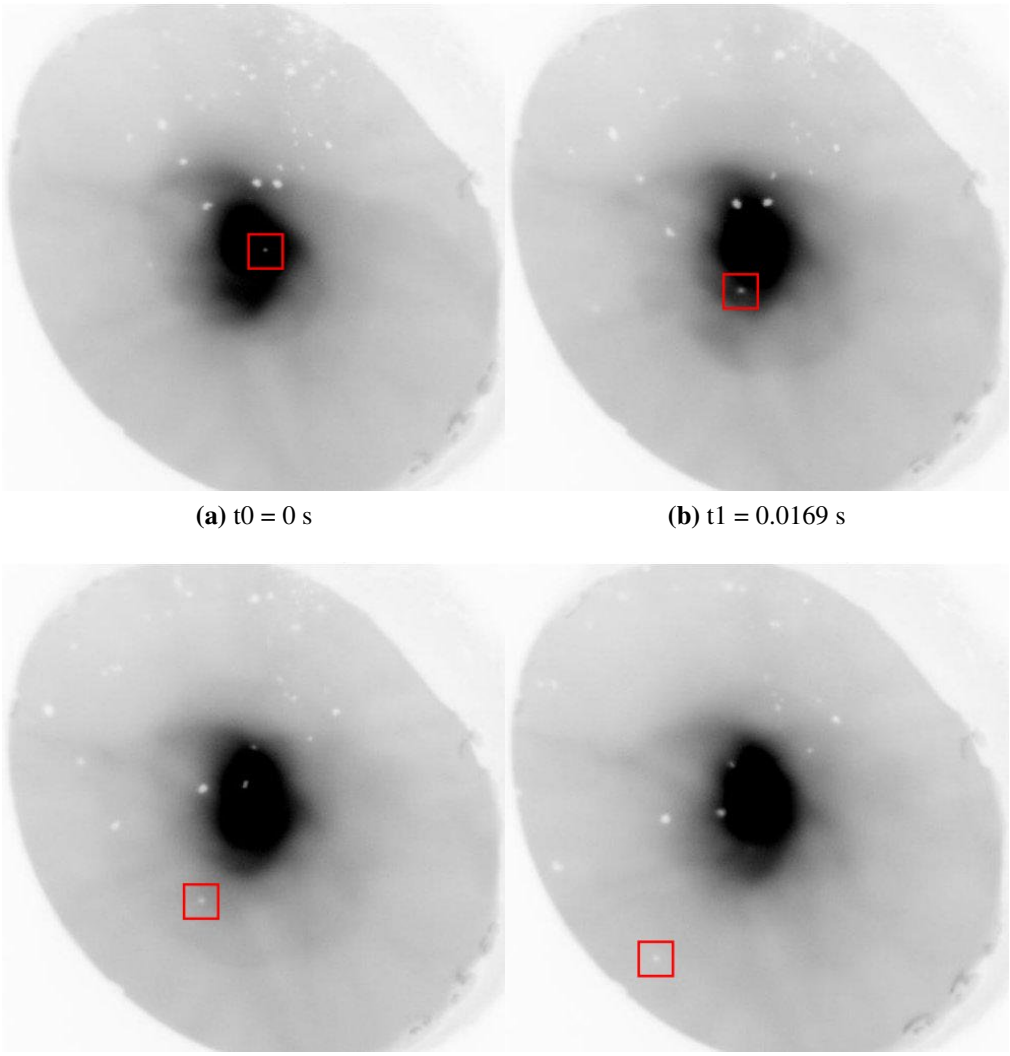

(a) t0 = 0 s **(b)** t1 = 0.0169 s

(c) t2 = 0.0339 s **(d)** t3 = 0.0508 s

Figure 6.8: Alumina Particles on the Surface of the Liquid Pool. Particle identified by the red square has been analyzed to determine fluid velocity on the pool surface. (Beam Pattern Radius: 3 mm; Beam Power: 13.0 kW. Aug 08)

After the experiment, the recorded video was analyzed frame by frame to ascertain the trajectory and velocity. Figure 6.8 shows an example of four frames at times of 0, 0.0169, 0.0339 and 0.0508 s after the particles were dropped onto the surface of the liquid pool. The grey scale in the images was inverted to provide better contrast for this analysis – e.g. hot regions on the surface appear black. The black region appearing approximately in the center of each image is the electron beam. The large grey ellipse-shaped region is the top surface

of the liquid pool. Note: the approximately circular pool appears as an ellipse because the camera is mounted at an angle relative to the top surface of the button. The average diameter of the liquid pool is 90 mm and the frame rate of the camera is 59 FPS. By measuring the distance traveled by the selected particle between two frames, the velocity for the selected particle is calculated. The selected alumina particle is marked with a red square in the images shown in Figure 6.8. In Figure 6.8(a), the selected particle starts near the center of the liquid pool. In the next series of frames (Figure 6.8(b) to 6.8(d)), the particle moves away from the center region towards the edge of the liquid pool. The four images show that the selected alumina particle is moving outward from the center of the liquid pool in a radial direction.

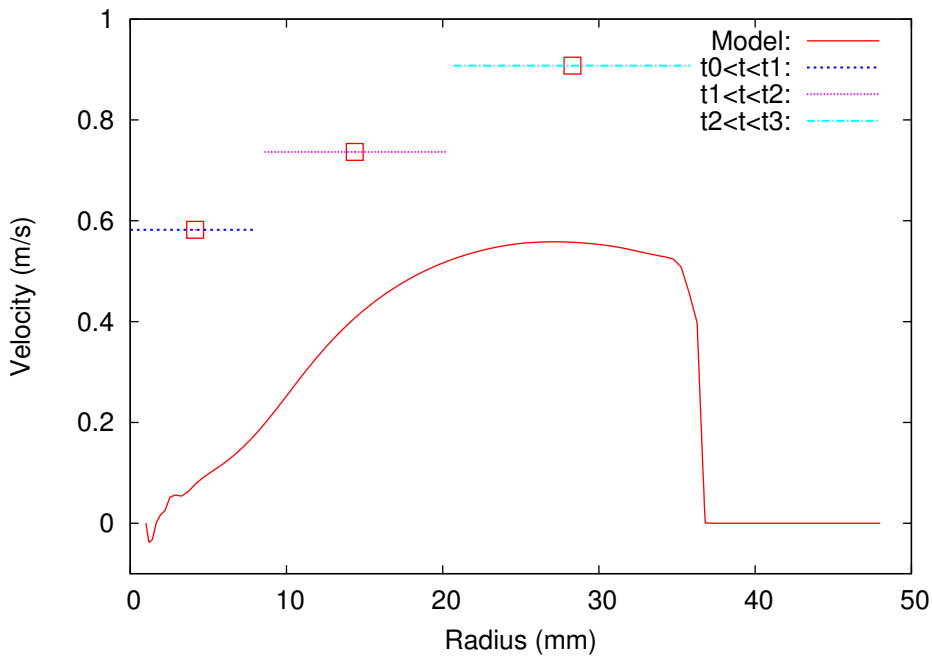

Figure 6.9: Comparison of Predicted and Measured Surface Velocities (Beam Pattern Radius: 3 mm; Beam Power: 13.0 kW. Aug 08)

The predicted surface velocity on the button sample is compared with the measured particle velocity in Figure 6.9. The measured velocities are shown as discrete points (squares) on the plot. The lines passing through each point represents the distance traveled by the particle in the time interval between subsequent frames. Therefore, the particle velocities

should be interpreted as an average over the distance traveled. The predicted velocity profile shows a similar direction (radial outward) and trend of increasing velocity with increasing radius to the measured particle velocities, suggesting that the fluid at the surface is accelerating towards the edge of the liquid pool. However, the predicted surface velocities are significantly lower than the measured particle velocities. One possible explanation for this discrepancy is that the alumina particles were fed onto the surface of the liquid pool by virtue of a screw feeder and an inclined chute (see Figure 4.1) and consequently will have an initial radial velocity component. This may explain the difference in velocity observed, particularly the high discrepancy close to the center of the button where the particles are introduced. In summary, the velocity predictions of the model may be classified as qualitatively correct and not quantitatively correct.

6.2 Effect of Various Flow Drivers

The model can be used to explore the effect of the various flow drivers present in the EB button melting process on the pool profile by activating or deactivating one or more of the drivers at a time. As previously described, the list of flow drivers includes thermal buoyancy, thermal Marangoni, compositional buoyancy and compositional Marangoni. In this analysis, the model has been run from the same initial condition with one or more of the specified flow drivers "activated" or "deactivated". Deactivation of a particular driver is realized by setting the relevant model parameter to zero – e.g. the surface tension coefficient with respect to temperature or the surface tension coefficient with respect to composition – or removing the relevant dependence – e.g. the density dependence on temperature or the density dependence on composition. The following cases have been run:

(1) Thermal buoyancy only,

(2) Compositional buoyancy only,

(3) Combined thermal and compositional buoyancy only,

(4) Thermal Marangoni only,

(5) Compositional Marangoni only,

(6) Combined thermal and compositional Marangoni only.

The results for cases 1 through 3 are presented in Figures 6.10(a) to 6.10(c), respectively, and the results for cases 4 through 6 in Figures 6.11(a) to 6.11(c), respectively.

With only thermal buoyancy considered and a radially decreasing temperature distribution from the center to the edge of the liquid pool, Figure 6.10(a) indicates a downward motion of the cooler and heavier fluid close to the edge of the liquid pool driven by the thermal buoyancy forces. As a result, the replenishing hotter and lighter liquid from the top center region flows radially outwards creating a clockwise recirculating flow cell in the liquid pool. Overall, a shallow and wide liquid pool with a smooth pool profile is formed.

Figure 6.10(b) shows the results for the case considering only compositional buoyancy flow. The center region at the surface of the liquid pool loses more aluminum relative to the peripheral region due to a high evaporation rate associated with high temperature and has relatively high densities. Driven by the compositional buoyancy forces, the heavier fluid at the top center region flows downwards, which is opposite in direction to the case with only thermal buoyancy flow being considered. This results in the replenishing fluid from the peripheral region flows towards the center of the liquid pool creating a counter-clockwise recirculating flow pattern and a deep, narrow pool profile.

In Figure 6.10(c), the pool profile and velocity vector plot for the case considering both thermal and compositional buoyancy closely resemble the case with only thermal buoyancy flow shown in Figure 6.10(a). The resemblance of the two cases indicates that the compositional buoyancy force is relatively weak compared with the thermal buoyancy force.

The results for the thermal Marangoni flow only case is shown in Figure 6.11(a). Since the surface tension of liquid Ti-6Al-4V decreases with increasing temperature and the center region on the top surface has the highest temperature, the thermal Marangoni force drives

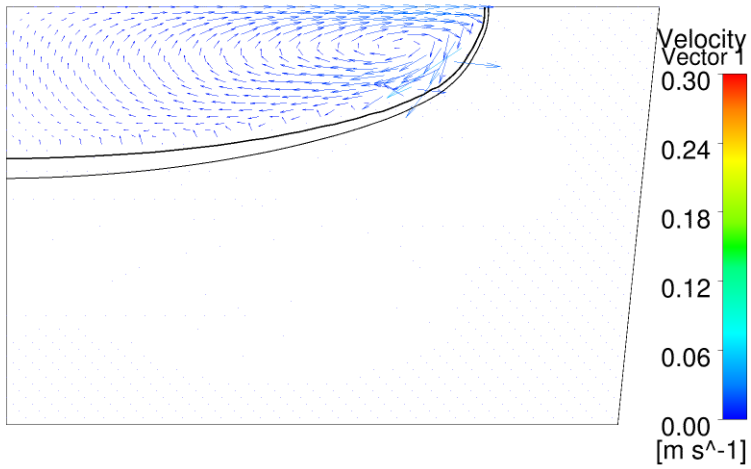

(a) Thermal Buoyancy Flow

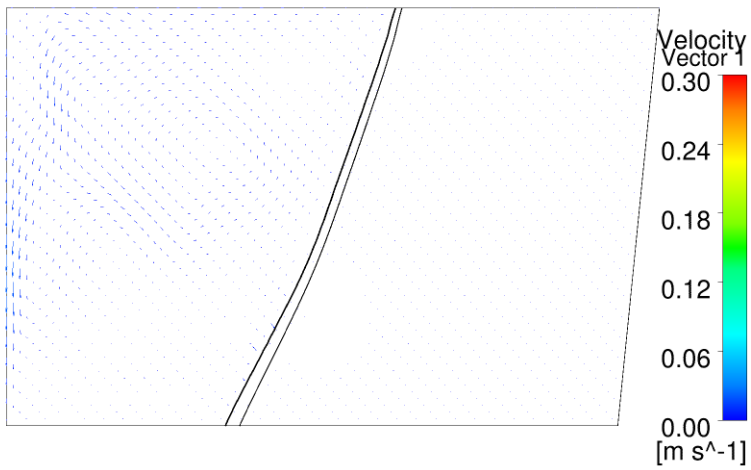

(b) Compositional Buoyancy Flow

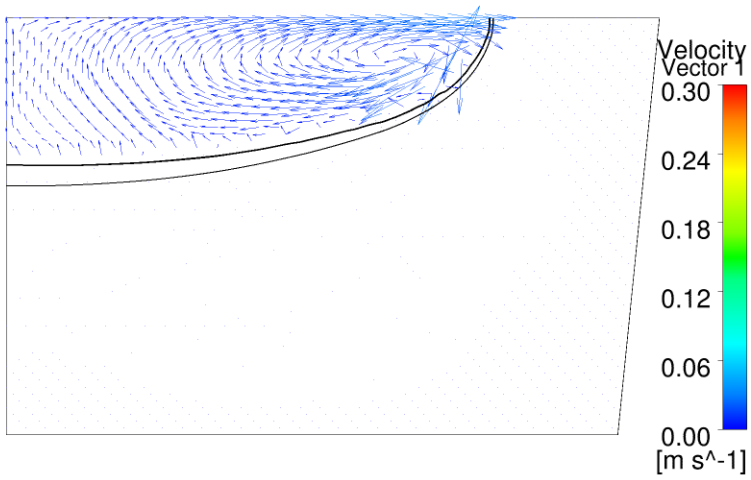

(c) Thermal and Compositional Buoyancy Flow

Figure 6.10: Effect of Thermal and Compositional Buoyancy Flow

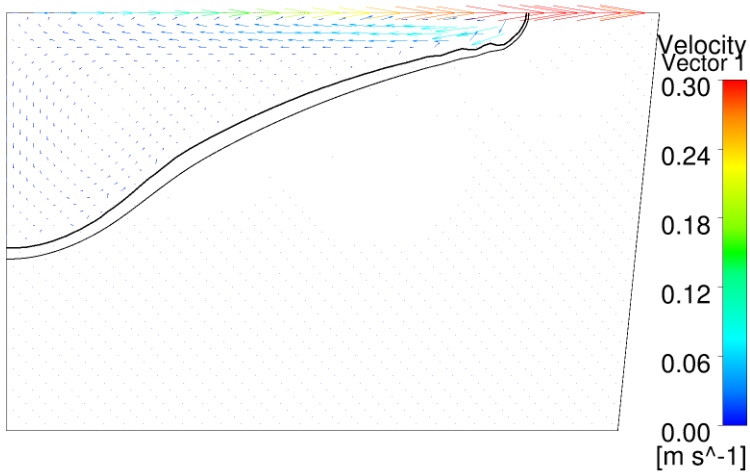

(a) Thermal Marangoni Flow

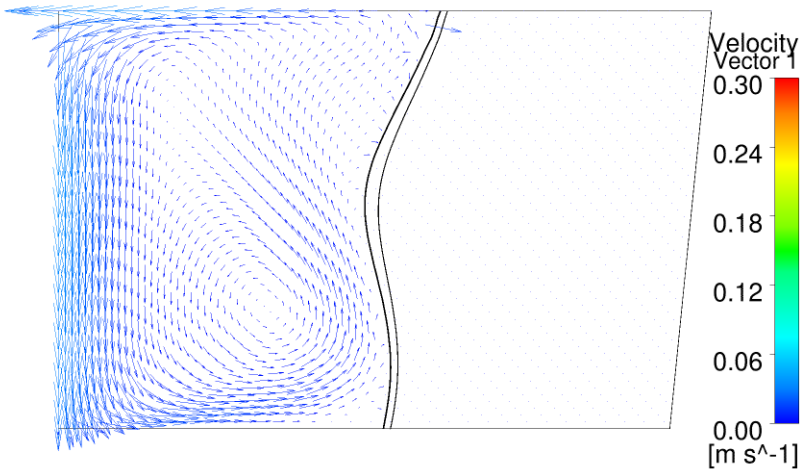

(b) Compositional Marangoni Flow

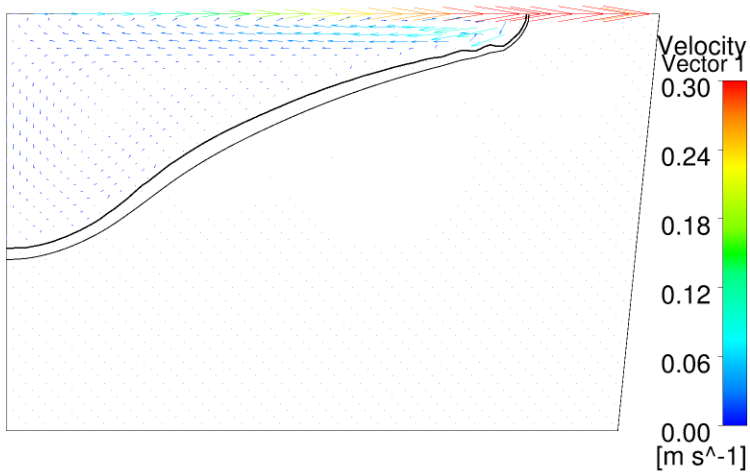

(c) Thermal and Compositional Marangoni Flow

Figure 6.11: Effect of Thermal and Compositional Marangoni Flow

the fluid at the surface to flow from the low surface tension region in the center to the high surface tension region close to the edge of the liquid pool. The result is a clockwise recirculating flow cell located just under the top surface. This cell, in turn, generates a second counter-clockwise recirculating flow cell toward the center and bottom of the liquid pool. Both of these recirculating cells combine to influence the pool profile, which adopts a more complex shape in which the curvature changes sign.

Figure 6.11(b) shows the results for the case where only compositional Marangoni flow is considered. The aluminum evaporation rate at the top surface is relatively high in the center region due to the radially decreasing temperature profile created by the electron beam. The surface fluid with decreased aluminum content in the center region on the top surface has relatively high surface tension while the material close to the edge of the liquid pool has relatively low surface tension. The fluid on the top surface is thus driven by the compositional Marangoni force to flow towards the center of the liquid pool and turns downwards upon reaching the center, creating a counter-clockwise recirculating flow pattern. This flow pattern resembles the case with only compositional buoyancy flow shown in Figure 6.10(b).

To provide additional insight, the transient results (at 10s, 20s and 30s) of the case with only compositional Marangoni flow are shown in Figure 6.12 as temperature and concentration contours with superimposed velocity vectors. At 10s, the region under the electron beam has the highest temperature and the lowest aluminum concentration. The surrounding surface fluid is driven by the compositional Marangoni force to flow towards this region creating a downward motion of the fluid with less aluminum content. At 20s, a radially decreasing temperature profile from the center to the edge has developed on the top surface of the liquid pool. Accordingly, the region with the lowest aluminum content appears in the top center of the liquid pool and a counter-clockwise recirculating flow pattern is formed. At 30s, with the continuing loss of aluminum through evaporation on the liquid surface and with high aluminum content liquid being brought up by the recirculating flow in the peripheral region, the concentration gradient at the top surface increases and the compositional

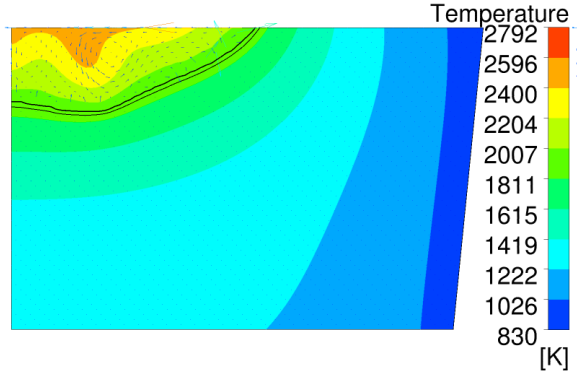

(a) Temperature Contour (t = 10 s)

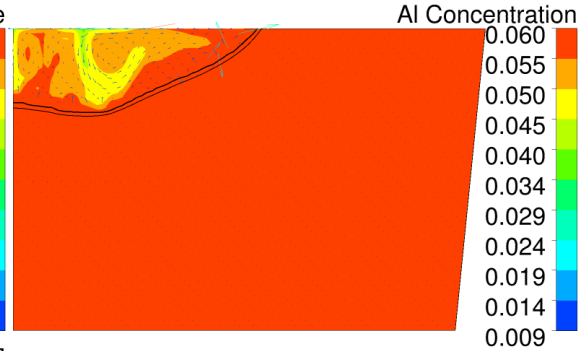

(b) Al Concentration Contour (t = 10 s)

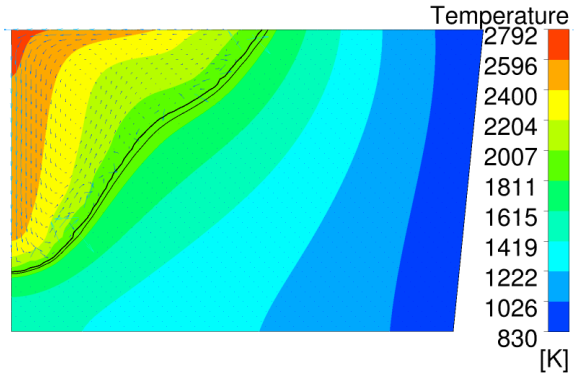

(c) Temperature Contour (t = 20 s)

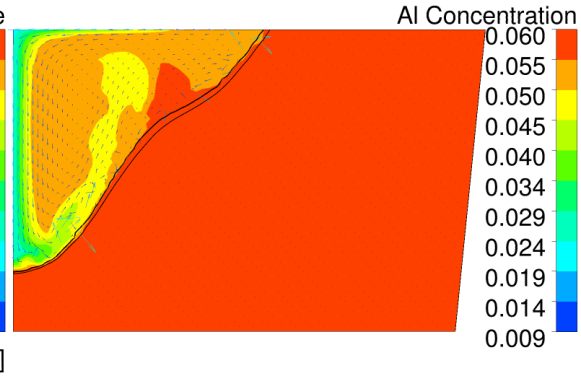

(d) Al Concentration Contour (t = 20 s)

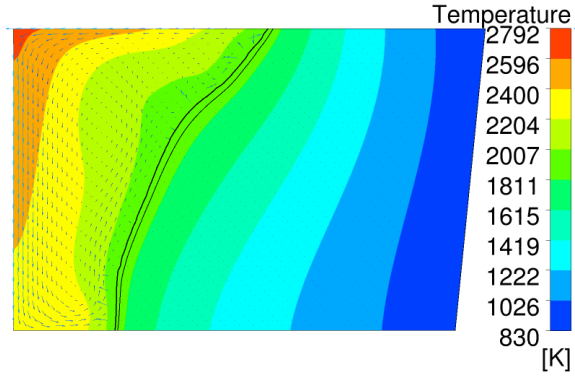

(e) Temperature Contour (t = 30 s)

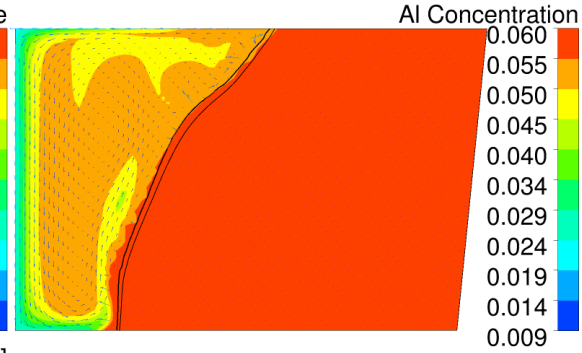

(f) Al Concentration Contour (t = 30 s)

Figure 6.12: Compositional Marangoni Flow at t = 10s, 20s and 30s

flow grows stronger with time. This flow has also led to the increase in pool depth.

Figure 6.11(c) shows that the flow pattern and the liquid pool profile with the thermal and compositional Marangoni forces combined. The resulting flow pattern is virtually identical to the results of the thermal only case shown in Figure 6.11(a). This indicates that compositional Marangoni force is relatively weak compared with thermal Marangoni force.

In summary, the pool profile in the button is more strongly affected by thermally induced forces compared with compositionally induced forces. Both of the thermally induced buoyancy and Marangoni forces combine to create a shallower and wider pool, which is consistent with observations.

6.3 Sensitivity Analysis

To further build confidence in the model, the sensitivity of the model predictions to changes in a number of the model parameters has been studied. The results of the analysis are presented as plots of temperature and velocity profiles in the button. By comparing these profiles, the impacts of uncertainties in these parameters are examined and the effect of each parameter on the modeling results is illustrated.

Table 6.2: Summary of Model Parameters Studied in Sensitivity Analysis

Model Parameter	Baseline	Variations	Unit
Mesh Size (Number of Elements)[1]	96×60	48×30, 144×90	–
Beam Power Efficiency Coeff. (η_{eb})	0.785	0.707, 0.864	–
Beam Pattern Radius (r_o)	15	10, 20	mm
Beam Focus (Standard Deviation, σ)	18	9, 25	mm
Heat Transfer Coefficient (h)[2]	$h \times 1.0$	$h \times 0.5$, $h \times 2.0$	$W/m^2/K$

[1] The minimum element size is 0.2 mm. The maximum element size is 0.537, 1.645 and 0.358 mm, respectively.
[2] Refer to Figure 5.7 for the value.

The model parameters examined together with the changes imposed to examine model sensitivity are summarized in Table 6.2. The baseline values are those that were found to give the best fit to the experimentally derived data. To conduct the sensitivity analysis,

only one parameter was changed at a time from its baseline value. All cases were run with the same initial conditions discussed in the model development section. The simulation time was chosen to be 300 seconds, which was 50 seconds longer than the minimum time required to develop a steady-state liquid pool. A constant beam power of 13.4 kW was used for this analysis.

Temperature profiles across the top surface and down the centerline of the button sample were plotted and compared as they are directly related to the depth and radius of the liquid pool. Velocity profiles across the top surface were plotted to study the effects of model parameters on flow conditions in the liquid pool.

6.3.1 Mesh Size

Additional information related to the mesh size sensitivity analysis are summarized in Table 6.3. The results are plotted in Figure 6.13 and summarized quantitatively in Table 6.4.

Table 6.3: Summary of Mesh Sizes Used in Sensitivity Analysis

Number of Elements	Type of Element	Min. Size (mm)	Max. Size (mm)	Time Step (s)	Run Time
96×60	Hexahedra	0.2	0.537	0.01	21 hr 55 min
48×30	Hexahedra	0.2	1.645	0.01	9 hr 51 min
144×90	Hexahedra	0.2	0.358	0.01	39 hr 11 min

Table 6.4: Sensitivity of Pool Depth, Pool Radius and Maximum Surface Velocity to Mesh Size

Number of Elements	Δ[1] (%)	Pool Depth D (mm)	ΔD (%)	Pool Radius R (mm)	ΔR (%)	Max. Velocity V_m (m/s)	ΔV_m (%)
96×60	Base	9.28	Base	36.35	Base	0.3061	Base
48×30	-50	11.93	+28.5	34.41	-5.3	0.3183	+4.0
144×90	+50	9.10	-1.9	36.62	+0.8	0.3119	+1.9

[1] The number of elements along a single edge of the geometry.

It is clear from this analysis that the cases run with 96×60 and 144×90 meshes predicted shallower and wider liquid pools than the case run with 48×30 mesh. The depth and

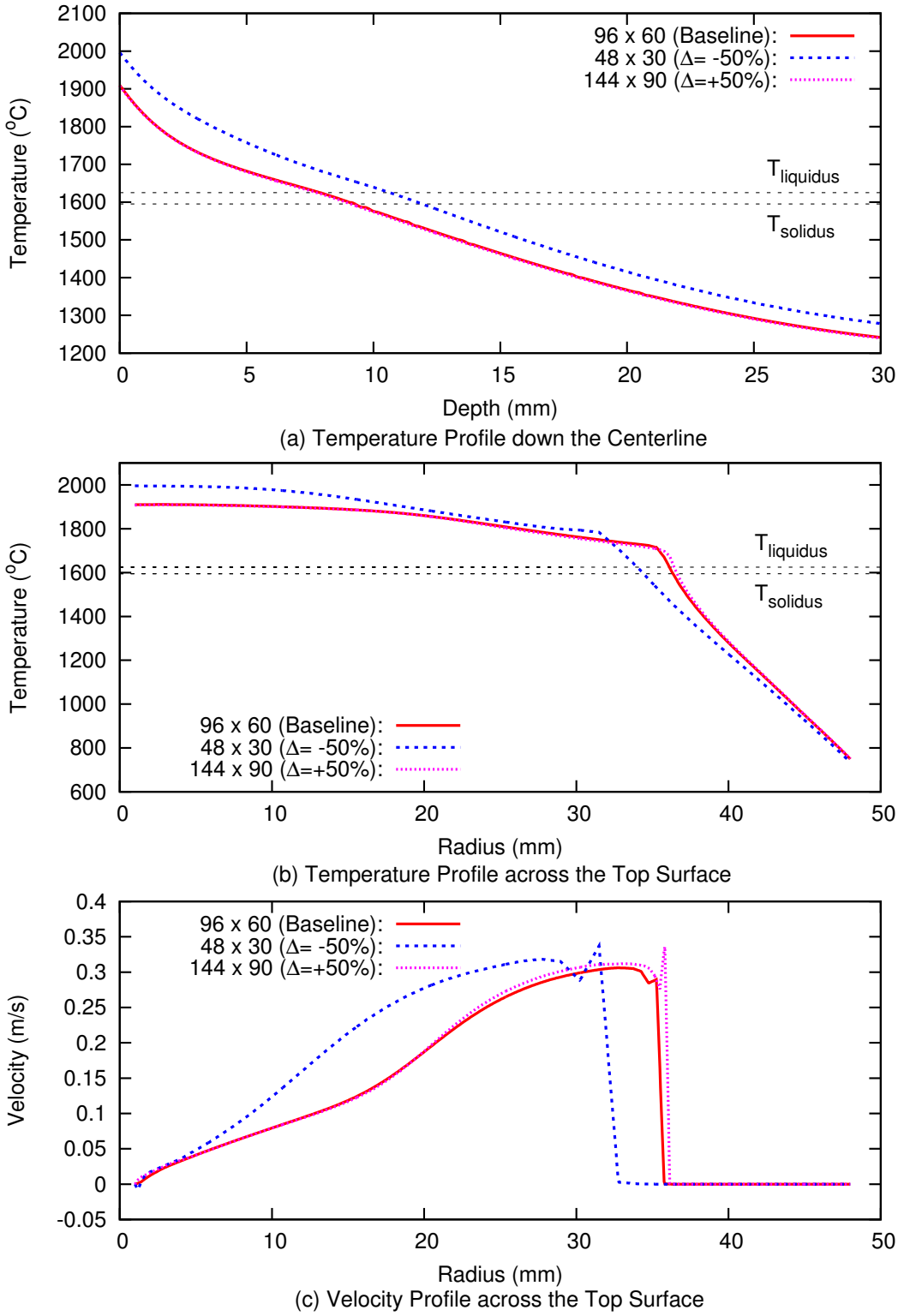

Figure 6.13: Sensitivity of Temperature and Velocity Profiles to Mesh Size

radius of the liquid pool predicted by the cases run with 96×60 and 144×90 meshes are almost identical with 1.9% and 0.8% differences in depth and radius, respectively. As seen in Figure 6.13(c), the velocity profile predicted by the case run with 48×30 mesh was also different from the other cases, although the calculated maximum surface velocity is only 5.3% lower than the baseline. Adding in a comparison of the execution time for the three cases, it would appear that the increased execution time associated with the 96×60 mesh is justified, whereas the increased execution time associated with the 144×90 mesh is not.

6.3.2 Boundary Conditions

There are two boundary conditions of concern with respect to the heat balance on the button that are complex and have been quantified by fitting the predictions of the model to experimentally derived data: 1) the EB heat flux applied to the top surface of the button; and 2) the heat transfer from the side of the button to the mold.

EB Heat Flux

The heat flux from the electron beam was approximated in the model by a two-dimensional normal distribution as described in Section 5.5.1. The total beam power used in the model was calculated by taking the product of the beam current and accelerating voltage, as measured during each experiment, and multiplying it by a beam power efficiency coefficient found in the literature. The beam pattern radius and size of the beam spot were estimated from video images taken from the experiment. The effect of the electron beam parameters was examined by varying the beam power efficiency coefficient, beam pattern radius and beam focus each at a time and then examining the effect of each on the temperature and velocity profiles predicted by the model.

The results of the sensitivity analysis for beam power efficiency are plotted in Figure 6.14 and summarized in Table 6.5. In addition to the base-case value of 0.785, efficiencies of 0.707 and 0.864, which represent a $\pm 10\%$ change, were also run with the model.

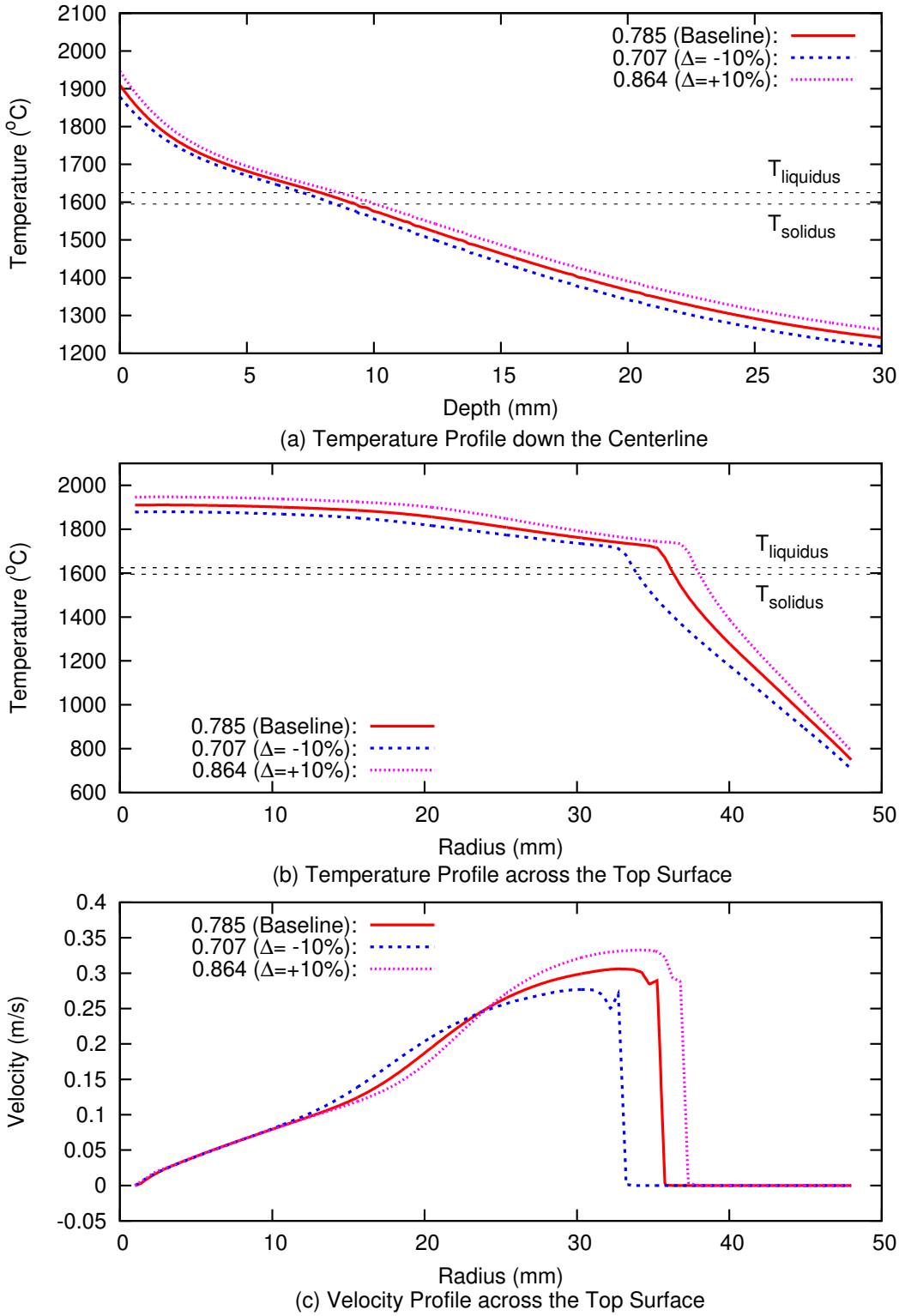

Figure 6.14: Sensitivity of Temperature and Velocity Profiles to Beam Power Efficiency Coefficient (η_{eb})

Table 6.5: Sensitivity of Pool Depth, Pool Radius and Maximum Surface Velocity to Beam Power Efficiency Coefficient (η_{eb})

η_{eb} (–)	Δ (%)	Pool Depth D (mm)	ΔD (%)	Pool Radius R (mm)	ΔR (%)	Max. Velocity V_m (m/s)	ΔV_m (%)
0.785	Base	9.28	Base	36.35	Base	0.3061	Base
0.707	-10	8.48	-8.7	33.97	-6.6	0.2770	-9.5
0.864	+10	10.00	+7.7	38.03	+4.6	0.3327	+8.7

As shown in Figure 6.14, the size of the liquid pool increases in both depth and radius with increased power input. Likewise, the maximum surface velocity also increases with beam power input. The changes in pool depth and radius are consistent with what would be expected. The increase in maximum surface velocity may be attributed to stronger thermally induced forces (buoyancy and Marangoni) acting on the liquid. As shown in Table 6.5, a $\pm$10% change in the EB power input results in a less than 10% change in pool depth, pool radius and maximum surface velocity.

The results of the sensitivity analysis for beam pattern radius are plotted in Figure 6.15 and summarized in Table 6.6. The variation in the beam pattern radius is 5 mm, which corresponds to approximately $\pm$33% of the baseline value. As shown in Figure 6.15(a) and (b), the temperature down the centerline and along the top surface of the button increases with the decreasing beam pattern radius. As a result, the liquid pool grows deeper and wider with the decreasing beam pattern radius. The temperature profiles shown in Figure 6.15(b) indicate that the temperature gradient on the top surface of the liquid pool, between the pool radii of 15 mm and 35 mm, increases with the decreasing beam pattern radius. Consequently, a significant increase in surface velocity with the decreasing beam pattern radius is observed between the pool radii of 15 mm and 35 mm in Figure 6.15(c). The maximum surface velocity increases by 15% on average each time the beam pattern radius is increased, as listed in Table 6.6. The increasing of surface velocity with decreasing beam pattern radius is attributed to the thermally induced flow which grows stronger as the temperature gradient increases in the liquid pool.

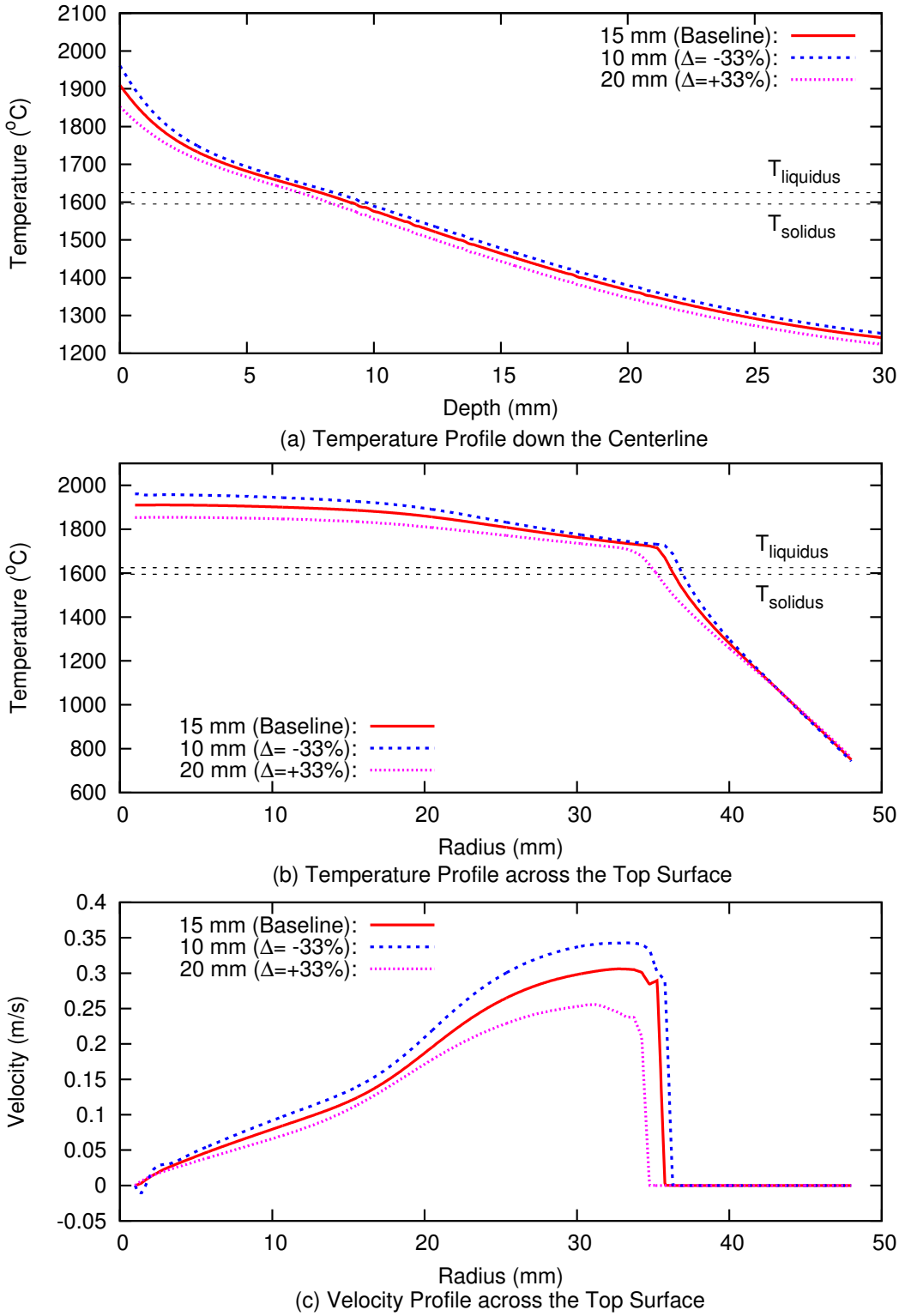

Figure 6.15: Sensitivity of Temperature and Velocity Profiles to Beam Pattern Radius (r_o)

Table 6.6: Sensitivity of Pool Depth, Pool Radius and Maximum Surface Velocity to Beam Pattern Radius (r_o)

r_o (mm)	Δ (%)	Pool Depth D (mm)	ΔD (%)	Pool Radius R (mm)	ΔR (%)	Max. Velocity V_m (m/s)	ΔV_m (%)
15	Base	9.28	Base	36.35	Base	0.3061	Base
10	-33	9.84	+6.0	36.94	+1.6	0.3429	+12.0
20	+33	8.41	-9.4	35.25	-3.0	0.2557	-16.5

The results of the sensitivity analysis for beam focus are plotted in Figure 6.16 and summarized in Table 6.7. Besides the baseline value of 18 mm, 9 and 25 mm, which represent a relatively focused beam and a more diffuse beam, respectively, were run with the model in this analysis.

Figure 6.16(a) and (b) indicate that the temperatures in the button sample increase significantly with the decreasing beam focus. The velocity profiles plotted in Figure 6.16(c) show that the surface velocity is very sensitive to variations in beam focus. The sensitivity of velocity to beam focus is attributed to the change in temperature gradient in the button, which drives the thermally induced flow in the liquid pool.

Table 6.7: Sensitivity of Pool Depth, Pool Radius and Maximum Surface Velocity to Beam Focus (σ)

σ (mm)	Δ (%)	Pool Depth D (mm)	ΔD (%)	Pool Radius R (mm)	ΔR (%)	Max. Velocity V_m (m/s)	ΔV_m (%)
18	Base	9.28	Base	36.35	Base	0.3061	Base
9	-50	12.19	+31.3	37.35	+2.7	0.4615	+50.8
25	+39	6.70	-27.8	30.73	-15.5	0.2012	-34.3

As shown in Table 6.7, the deepest and widest liquid pool is seen in the case with $\sigma =$ 9 mm, which also has the highest maximum surface velocity among the three listed cases. With -50% and $+39\%$ changes in beam focus, the variations in maximum surface velocity are $+50.8\%$ and -34.3%, respectively.

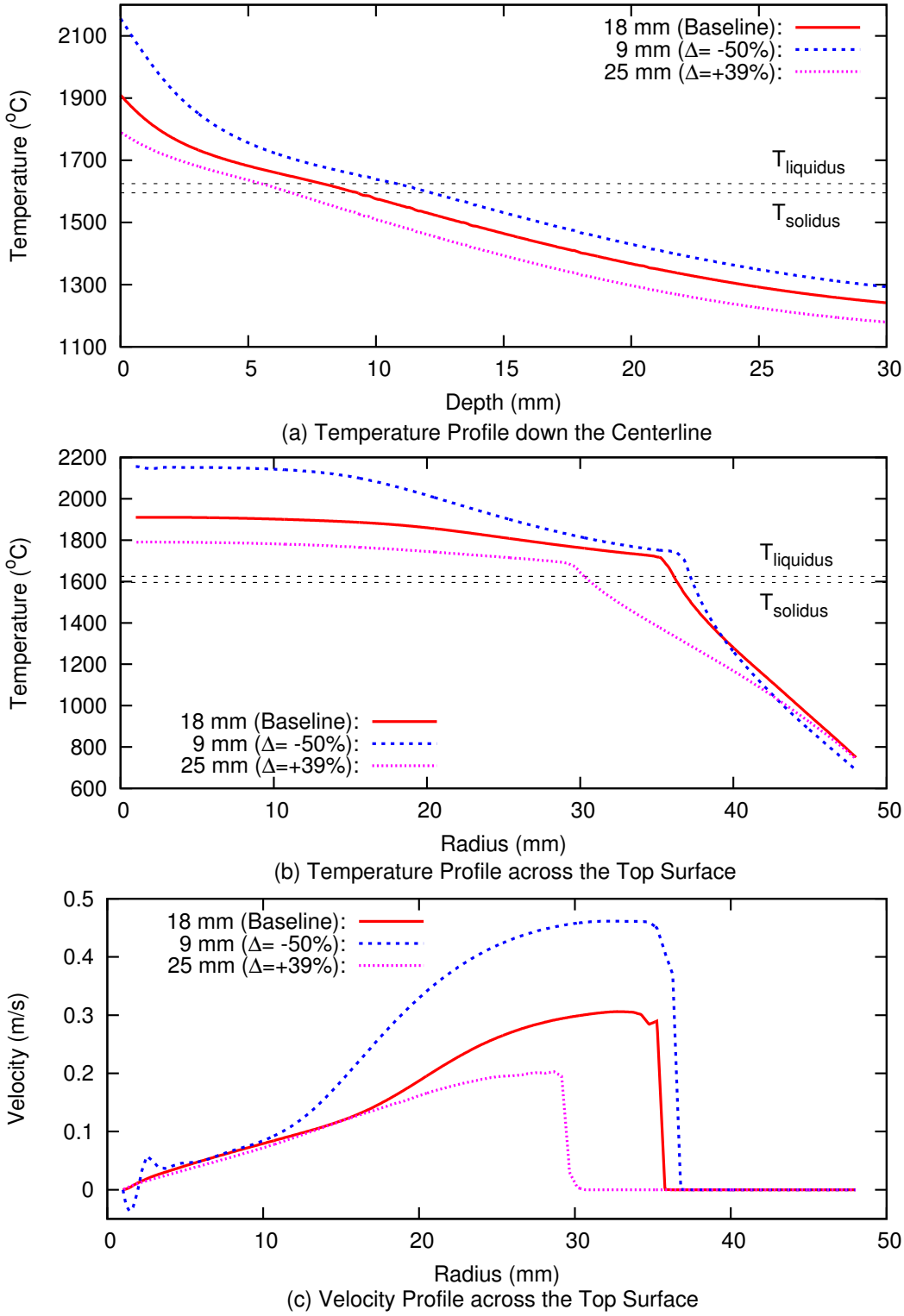

Figure 6.16: Sensitivity of Temperature and Velocity Profiles to Beam Focus (σ)

Heat Transfer Coefficient

The heat transfer from the side of the button to the mold was described in the model by the heat transfer coefficient applied to the side surface of the domain. The value of the heat transfer coefficient used in the model was determined by fitting predicted cooling curves to temperature data measured during the experiments. A sensitivity analysis has been performed to evaluate the impact of heat transfer coefficient on the modeling results.

The results of the sensitivity analysis for heat transfer coefficient are plotted in Figure 6.17 and summarized in Table 6.8. The baseline value of the heat transfer coefficient (refer to Figure 5.7) was reduced by half and doubled in this analysis, respectively.

Figure 6.17(a) and (b) indicate that the temperatures in the liquid pool are less sensitive to variations in heat transfer coefficient than the temperatures in the solid region. The region that is the closest to the side of the button is the most sensitive to variations in heat transfer coefficient. This result is consistent with the fact that heat is extracted from the button predominantly through its side surface and the region in proximity to this boundary will be the most affected. The temperature profiles suggest that the heat transfer in the liquid pool is governed by fluid flow since the liquid region is not as sensitive to variations in heat transfer coefficient as the solid region. The lack of sensitivity to variations in heat transfer coefficient in the liquid region can also be inferred from the velocity profiles shown in Figure 6.17(c). The velocities between pool radii of 15 mm and 25 mm are likely affected by pool radius rather than temperature variations.

Table 6.8: Sensitivity of Pool Depth, Pool Radius and Maximum Surface Velocity to Heat Transfer Coefficient (h)

h (W/m^2/^{o}C)	Δ (%)	Pool Depth D (mm)	ΔD (%)	Pool Radius R (mm)	ΔR (%)	Max. Velocity V_m (m/s)	ΔV_m (%)
$h \times 1.0$	Base	9.28	Base	36.35	Base	0.3061	Base
$h \times 0.5$	-50	10.07	+8.5	38.51	+6.0	0.3158	+3.2
$h \times 2.0$	+100	8.87	-4.4	35.29	-2.9	0.3002	-1.9

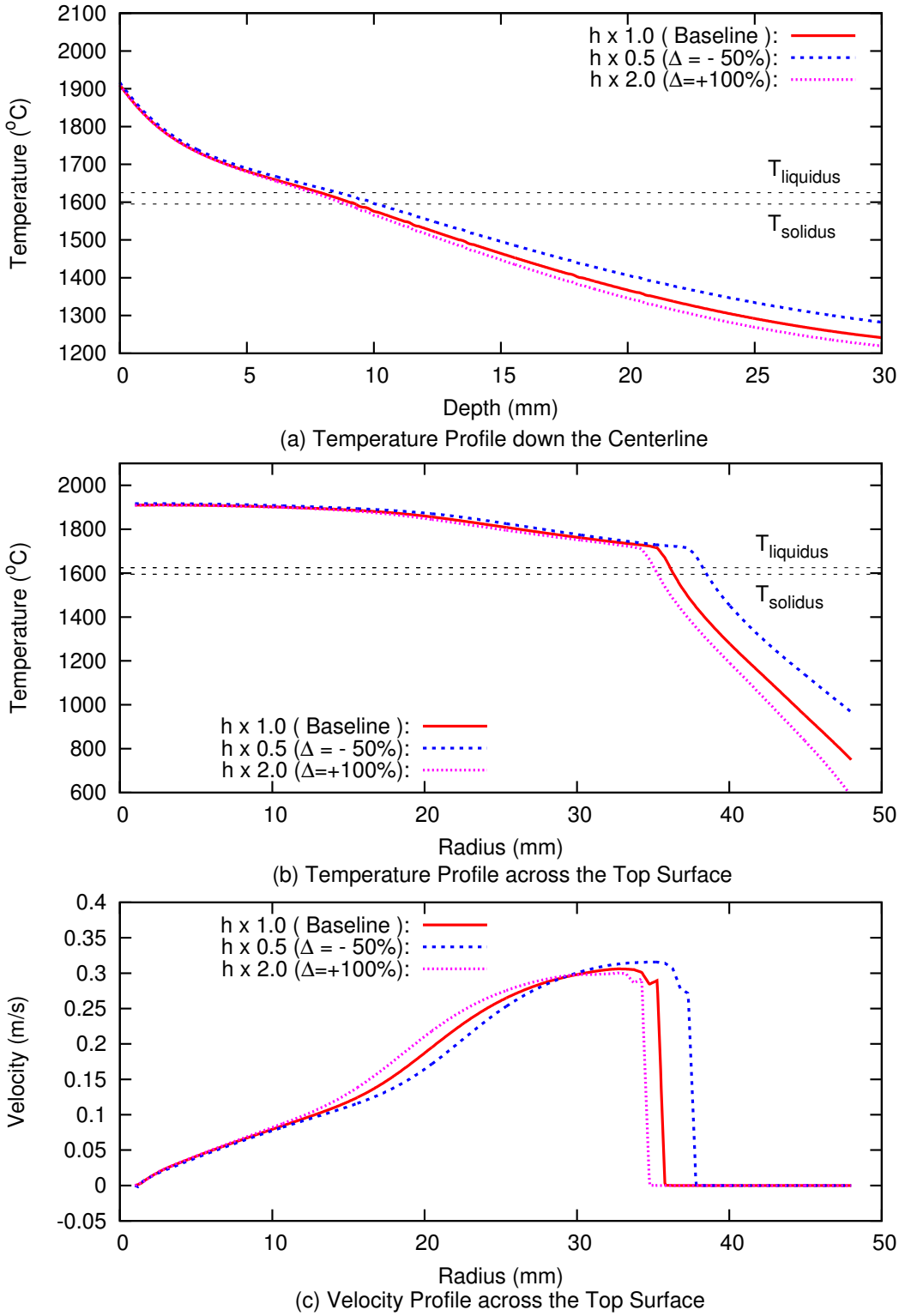

Figure 6.17: Sensitivity of Temperature and Velocity Profiles to Heat Transfer Coefficient (h)

As shown in Table 6.8, with the heat transfer coefficient being reduced by half, the pool depth and pool radius increase by 8.5% and 6.0%, respectively. With the heat transfer coefficient being doubled, the pool depth and pool radius decrease by 4.4% and 2.9%, respectively. The changes of maximum surface velocity in both cases are within 4%.

Chapter 7

Conclusions and Future Work

7.1 Summary and Conclusions

A comprehensive thermal-fluid-compositional model has been developed to predict the temperature, velocity and concentration fields during the Electron Beam Button Melting (EBBM) of Ti-6Al-4V. The fluid flow driving forces that are active in the melt pool, including thermal buoyancy, thermal Marangoni, compositional buoyancy and compositional Marangoni, were incorporated in the model. Lab-scale EBBM experiments were conducted to provide suitable data for model verification. Model predictions have been compared with experimental results in temperature, pool profile, surface velocity and concentration profile. The effect of aluminum evaporation on the flow conditions and pool profile have been assessed using the model.

The comparison of the temperature results indicates that the model is capable of predicting the temperature distribution in the button sample during the EB melting process. The temperature evolution including the release of latent heat from liquid to solid and β to α phase transformations was produced by the model. The model correctly predicted the depth, radius and shape of the liquid pool in the button sample.

The concentration distribution of aluminum in the button sample presents a uniform

concentration profile in the liquid pool. The model has shown the ability to characterize the evaporation of aluminum in the melting process and to predict the final aluminum concentration after the melting experiments.

The velocity measurements showed the melt at the surface of the liquid pool was flowing and accelerating in the outward radial direction from the center towards the edge of the liquid pool which is in agreement with the predicted surface velocity profile. Due to experimental difficulties, the velocity measurements are limited to a melting experiment with a highly centered beam pattern. Compared with the circular beam pattern used in the other experiments, the centered beam pattern led to higher temperature gradients on the surface of the button which resulted in stronger fluid flow at the surface of the melt pool.

Flow analysis has shown that the buoyancy and Marangoni flow driven by concentration variations induced by the evaporation of aluminum are in the inward radial direction from the edge to the center at the surface of the liquid pool. Thermal buoyancy and thermal Marangoni flow are in the outward radial direction from the center to the edge at the surface of the liquid pool under the heat flux distribution applied in this study. Both thermally induced buoyancy and Marangoni forces combine to create a shallow and wide liquid pool as observed in the experiments. Thus, the incorporation of Marangoni flow in the model is crucial to predicting the liquid pool profile and, compared with thermally induced flow, compositional flow has little effect on pool profile under current experimental conditions.

The model showed reasonable sensitivity to the various model parameters including mesh size and boundary conditions. A 96×60 mesh was justified based on the accuracy of the predictions and the execution time. The beam power efficiency coefficient, beam pattern radius and beam focus which define the electron beam heat flux intensity and distribution had a significant effect on the temperature distribution in the button sample and the surface velocity profiles in the liquid pool. The temperatures in the solid region are more sensitive to the variations in heat transfer coefficient than the temperatures in the liquid pool.

7.2 Future Work

The velocity measurements performed in this research were limited by the frame rate of the camera used in the experiment and the method used to introduce the alumina particles onto the liquid surface. A camera with a higher frame rate should be used to improve the accuracy of the velocity measurements in the future. The aluminum particles should be dropped onto the liquid pool from a lower position to reduce the initial velocity.

The effects of compositional buoyancy and compositional Marangoni flow identified in this research should be further investigated by artificially introducing aluminum or aluminum alloys into the titanium liquid pool. With the aid of larger local concentration gradients, the effect of compositional flow on the temperature and velocity fields should become more apparent as the surface fluid driven by aluminum concentration variations will flow in the outward radial direction away from the aluminum rich region.

The research presented here was focused on lab-scale Electron Beam Button Melting process conducted in a small-scale EB furnace available at UBC. The fluid phenomena identified and modeled in the EBBM process are applicable to the industrial Electron Beam Cold Hearth Remelting process. With proper adjustment in domain, boundary conditions and initial conditions, the model developed in this research may be applied to the industrial EBCHR practice.

Bibliography

[1] Kenneth C Mills. *Recommended Values of Thermophysical Properties for Selected Commercial Alloys*. Woodhead Publishing Ltd., Cambridge England, 2002.

[2] Ana Kostov and Bernd Friedrich. Predicting thermodynamics stability of crucible oxides in molten titanium and titanium alloys. *Computational Materials Science*, 38:374–385, 2006.

[3] G. Lutjering and J.C. Williams. *Titanium 2nd Edition*. Springer, New York, 2007.

[4] Tomoo Isawa, Hideo Nakamura, and Katsuhiko Murakami. Aluminum evaporation from titanium alloys in eb hearth melting process. *ISIJ International*, 32:607–615, 1992.

[5] David W. Tripp. *Modelling Power Transfer in Electron Beam Heating of Cylinders*. PhD thesis, The University of British Columbia, Vancouver, 1994.

[6] Ghassan Ghazal, Pierre Chapelle, Alain Jardy, Julien Jourdan, and Yvon Millet. Dissolution of high density inclusions in titanium alloys. *ISIJ International*, 52:1–9, 2012.

[7] Alec Mitchell. Melting, casting and forging problems in titanium alloys. *Materials Science and Engineering*, A243:257–262, 1998.

[8] Xuanhe Zhao. *Mathematical Modeling of Electron Beam Cold Hearth Casting of Titanium Alloy Ingots*. Master's Thesis, The University of British Columbia, Vancouver, 2006.

[9] S. V. Akhonin, N. P. Trigub, V. N. Zamkov, and S. L. Semiatin. Mathematical modeling of aluminum evaporation during Electron Beam Cold Hearth Melting of Ti-6Al-4V ingots. *Metallurgical and Materials Transactions B*, 34B:447–454, 2003.

[10] M. Ritchie, P.D. Lee, A. Mitchell, S.L. Cockcroft, and T. Wang. X-ray-based measurement of composition during Electron Beam melting of AISI 316 stainless steel: Part II. evaporative processes and simulation. *Metallurgical and Materials Transactions A*, 34A:863–877, 2003.

[11] Shiro Watakabe, Ken'ichiro Suzuki, and Koji Nishikawa. Control of chemical compositions of Ti-6Al-4V alloy during melting by Electron Beam furnace. *ISIJ International*, 32:625–629, 1992.

[12] Hideo Nakamura and Alec Mitchell. The effect of beam oscillation rate on al evaporation from a Ti-6Al-4V alloy in the Electron Beam melting process. *ISIJ International*, 32:583–592, 1992.

[13] Ken ichiro Suzuki and Siro Watakabe. Melting and precision casting of Ti-6Al-4V alloy by use of Electron Beam furnace. *Metals and Materials International*, 9:359–367, 2003.

[14] P.D. Lee, P.N. Quested, and M. McLean. Modelling of Marangoni effects in electron beam melting. *Philosophical Transactions of the Royal Society A*, 356:1027–1043, 1998.

[15] P. F. Paradis, T. Ishikawa, and S. Yoda. Non-contact measurements of surface tension and viscosity of niobium, zirconium and titanium using and electrostatic levitation furnace. *International Journal of Thermophysics*, 23:825–841, 2002.

[16] I. Egry, D. Holland-moritz, R. Novakovic, et al. Thermophysical properties of liquid AlTi-based alloys. *International Journal of Thermophysics*, 31:949–965, 2010.

[17] Ragnhild Aune, Livio Battezzati, Rob Brooks, et al. Surface tension and viscosity of industrial alloys from parabolic flight experiments - results of the Thermolab project. *Microgravity Science and Technology*, XVI-1:11–14, 2005.

[18] Rainer K. Wunderlich. Surface tension and viscosity of industrial Ti-Alloys measured by the oscillating drop method on board parabolic flights. *High Temperature Materials and Processes (Telaviv, Israel)*, 27-6:401–412, 2008.

[19] B. J. Keene. Review of data for the surface tension of pure metals. *International Materials Reviews*, 38(4):157–192, 1993.

[20] Y. P. Lei, Hidekazu Murakawa, Y. W. Shi, and X. Y. Li. Numerical analysis of the competitive influence of Marangoni flow and evaporation on heat surface temperature and molten pool shape in laser surface remelting. *Computational Materials Science*, 21:276–290, 2001.

[21] S. L. Semiatin, V. G. Ivanchenko, S. V. Akhonin, and O. M. Ivasishin. Diffusion models for evaporation losses during Electron-Beam melting of Alpha/Beta-Titanium alloys. *Metallurgical and Materials Transactions B*, 35B:235–245, 2004.

[22] V. G. Ivanchenko, O. M. Ivasishin, and S. L. Semiatin. Evaluation of evaporation losses during Electron Beam melting of Ti-Al-V alloys. *Metallurgical and Materials Transactions B*, 34B:911–915, 2003.

[23] W. Shyy, Y. Pang, G. B. Hunter, et al. Effect of turbulent heat transfer on continuous ingot solidification. *Journal of Engineering Materials and Technology*, 115:8–16, 1993.

[24] A. Powell, J. Van Den Avyle, B. Damkroger, J. Szekely, and U. Pal. Analysis of multicomponent evaporation in Electron Beam melting and refining of titanium alloys. *Metallurgical and Materials Transactions B*, 28B:1227–1239, 1997.

[25] J. P. Bellot, E. Hess, and D. Ablitzer. Aluminum volatilization and inclusion removal in the Electron Beam Cold Hearth Melting of ti alloys. *Metallurgical and Materials Transactions B*, 31B:845–854, 2000.

[26] M. Ritchie, P.D. Lee, A. Mitchell, S.L. Cockcroft, and T. Wang. X-ray-based measurement of composition during Electron Beam melting of AISI 316 stainless steel: Part I. experimental setup and processing of spectra. *Metallurgical and Materials Transactions A*, 34A:851–861, 2003.

[27] Tao Meng. *Factors Influencing the Fluid Flow and Heat Transfer in Electron Beam Melting of Ti-6Al-4V*. Master's Thesis, The University of British Columbia, Vancouver, 2009.

[28] *EH 30/20 EB Gun Technical Documentation*. VON ARDENNE, Germany, 1992.

[29] *Electron Beam Melting Furnace: Another User Manual*. Denis Favez, Vancouver, 2009.

[30] *ASTM E230-03 Standard Specification and Temperature-Electromotive Force (EMF) Tables for Standardized Thermocouples*. ASTM International, West Conshohocken, PA, 2003.

[31] *ANSYS CFX-Solver Theory Guide*. ANSYS, Inc., PA, 2009.

[32] Riley Shuster. *Modeling of the Composition Variation during Casting of Titanium Alloy Ingots Following Electron Beam Cold Hearth Remelting*. MERC 2008, The University of British Columbia, Vancouver, 2008.

[33] M. C. Flemings. Solidification processing. *Metallurgical Transactions*, 5:2121–2134, 1974.

[34] Malcolm D. Lane. *A Coupled Thermal-Fluid Flow Model of the Horizontal Direct Chill Casting Process for T-Ingot*. Master's Thesis, The University of British Columbia, Vancouver, 2004.

[35] W. F. Gale and T. C. Totemeier, editors. *Smithells Metals Reference Book, 8th Edition.* Elsevier Butterworth-Heinemann, Oxford, 2004.

[36] M. Boivineau, C. Cagran, D. Doytier, et al. Thermophysical properties of solid and liquid Ti-6Al-4V alloy. *International Journal of Thermophysics*, 27-2:507–529, 2006.

[37] Mark Thomas Ritchie. *EDX Investigation of Evaporative Losses during the EB Melting of SS316*. Doctoral Thesis, The University of British Columbia, Vancouver, 1997.

[38] L. C. Chhabildas, W. D. Reinhart, T. F. Thornhill, and J. L. Brown. Shock-induced vaporization in metals. *International Journal of Impact Engineering*, 33:158–168, 2006.

[39] Irving Langmuir. The vapor pressure of metallic tungsten. *The Physical Review*, II-5:329–342, 1913.

[40] S. L. Semiatin, V. G. Ivanchenko, S. V. Akhonin, and O. M. Ivasishin. Diffusion models for evaporation losses during Electron-Beam melting of Alpha/Beta-Titanium alloys. *Metallurgical and Materials Transactions B*, 35B:235–245, 2003.

[41] Yunus A. Cengel. *Heat Transfer: A Practical Approach*. McGraw-Hill Inc., New York, 2003.

[42] Scott A. Socolofsky and Gerhard H. Jirka. *CVEN 489-501: Special Topics in Mixing and Transport Processes in the Environment*. TX, 2005.

[43] Z. Yang, S. Sista, J. W. Elmer, and T. Debroy. Three dimensional Monte Carlo simulation of grain growth during GTA welding of titanium. *Acta Materialia*, 48:4813–4825, 2000.

[44] *Type C Revised Thermocouple Reference Table*. Omega Engineering, Inc., Stamford, Connecticut.

Appendix A

Inverse Polynomial for Type-C Thermocouples

As type-C thermocouples are not directly supported by the DAQ system drivers, voltage measurements were applied to type-C thermocouples during the experiments. The conversion to temperature and the Cold Junction Compensation (CJC) were performed in the LabVIEW program.

The following inverse polynomial for type-C thermocouples was used to convert thermoelectric voltage to temperature[30]:

$$T = a_0 + a_1 E + a_2 E^2 + a_3 E^3 \ldots a_n E^n \tag{A.1}$$

where T is the temperature (^{o}C), E is the thermoelectric voltage (Electromotive Force or EMF, in mV), and $a_0, a_1, a_2, \ldots a_n$ are the coefficients given in Table A.1.

With a reference junction at 0 ^{o}C, the temperature calculated using the above polynomial agreed well with the values given in the manufacturer's thermocouple reference table (within $\pm$ 0.5^{o}C)[44]. In the experiment, the cold junction temperature was assumed to be room temperature, which was measured with a laboratory thermometer prior to the start of

Table A.1: Coefficients of Inverse Polynomials for Type-C Thermocouples[30]

Temperature Range	Coefficients
0 °C to 2315 °C (Reference Junction at 0 °C)	$a_0 = 0.000\,000\,00$
	$a_1 = 7.412\,473\,26 \times 10^{1}$
	$a_2 = -4.280\,828\,13$
	$a_3 = 5.211\,389\,20 \times 10^{-1}$
	$a_4 = -4.574\,872\,01 \times 10^{-2}$
	$a_5 = 2.805\,782\,84 \times 10^{-3}$
	$a_6 = -1.131\,451\,37 \times 10^{-4}$
	$a_7 = 2.854\,896\,84 \times 10^{-6}$
	$a_8 = -4.076\,438\,28 \times 10^{-8}$
	$a_9 = 2.513\,580\,71 \times 10^{-10}$

every experiment. The cold junction temperature was then converted to its equivalent thermoelectric voltage and added to the voltage readings of the thermocouples before the final conversion to temperature.